

# Full top quark mass dependence in Higgs boson pair production at NLO

---

**S. Borowka,<sup>a</sup> N. Greiner,<sup>a</sup> G. Heinrich,<sup>b</sup> S. P. Jones,<sup>b</sup> M. Kerner,<sup>b</sup> J. Schlenk,<sup>b</sup> T. Zirke<sup>b</sup>**

<sup>a</sup>*Institute for Physics, Universität Zürich, Winterthurerstr.190, 8057 Zürich, Switzerland*

<sup>b</sup>*Max-Planck-Institute for Physics, Föhringer Ring 6, 80805 München, Germany*

**ABSTRACT:** We study the effects of the exact top quark mass-dependent two-loop corrections to Higgs boson pair production by gluon fusion at the LHC and at a 100 TeV hadron collider. We perform a detailed comparison of the full next-to-leading order result to various approximations at the level of differential distributions and also analyse non-standard Higgs self-coupling scenarios. We find that the different next-to-leading order approximations differ from the full result by up to 50 percent in relevant differential distributions. This clearly stresses the importance of the full NLO result.

**KEYWORDS:** QCD, Higgs, two-loop, top quark mass, future colliders

---

## Contents

<b>1</b>	<b>Introduction</b>	<b>1</b>
<b>2</b>	<b>Details of the calculation</b>	<b>4</b>
2.1	Amplitude structure	4
2.2	Leading Order cross section	6
2.2.1	Heavy top limit	7
2.3	NLO cross section	7
2.3.1	Calculation of the virtual two-loop amplitude	8
2.3.2	Real radiation	16
2.4	Validation of the calculation and expansion in $1/m_t$	17
2.4.1	Expansion in $1/m_t^2$	17
2.4.2	Checks of the calculation	18
<b>3</b>	<b>Phenomenological results</b>	<b>20</b>
3.1	Setup and total cross sections	20
3.2	NLO distributions	20
3.3	Sensitivity to the triple Higgs coupling	27
<b>4</b>	<b>Conclusions</b>	<b>32</b>

---

## 1 Introduction

After the discovery of a boson [1, 2] whose characteristics have so far been consistent with the Standard Model Higgs boson, it is a primary goal of the LHC and future colliders to further scrutinize its properties. In particular, the form of the Higgs potential needs to be reconstructed by experimental measurements, in order to confirm the mechanism of electroweak symmetry breaking postulated by the Standard Model. One of the parameters entering the Higgs potential, the mass of the Higgs boson, already has been measured to an impressive precision [3]. The other parameter, the Higgs boson self-coupling, is more difficult to constrain, as it requires the production of at least two Higgs bosons. The cross sections for Higgs boson pair production at the LHC are about three orders of magnitude smaller than the ones for single Higgs production.

The dominant production channel is the gluon fusion channel, as for single Higgs boson production at the LHC.

In the gluon fusion channel, there are two categories of contributions to di-Higgs production: either a virtual Higgs boson, produced by the same mechanism as in single Higgs production, is decaying into a Higgs boson pair, involving the self-coupling  $\lambda_{hhh}$ , or the two Higgs bosons are both directly radiated from a heavy quark. At leading order (LO), these two mechanisms can be attributed to “triangle” and “box” contributions, respectively. However, at NLO, i.e. at the level of two-loop diagrams, the diagram topologies are more complicated, such that the association of “triangle diagrams” to diagrams containing the self-coupling  $\lambda_{hhh}$  becomes invalid.

The Higgs boson pair production cross section is additionally suppressed by the fact that there is destructive interference between contributions containing the Higgs boson self-coupling and the ones containing only Yukawa couplings to heavy quarks, and that for larger values of  $\sqrt{\hat{s}}$ , the contributions with an s-channel virtual Higgs boson propagator are strongly suppressed.

Therefore, narrowing the window of possible values for the triple-Higgs coupling experimentally will have to wait until the high-luminosity run of the LHC [4–6], if Standard Model rates are assumed. However, the Higgs boson pair production rate could be modified by physics beyond the Standard Model (BSM), and hence it is important to be able to distinguish BSM effects from Standard Model higher order corrections. In this paper we will study the effects of a modified Higgs boson self-coupling and show that the Higgs boson invariant mass distribution is quite sensitive to changes in  $\lambda_{hhh}$ , as such changes modify the interference pattern.

Both ATLAS and CMS have published measurements of Higgs boson pair production in the decay channels  $\gamma\gamma b\bar{b}$  [7–10],  $b\bar{b}b\bar{b}$  [9, 11–14],  $\gamma\gamma WW^*$ ,  $b\bar{b}WW^*$ ,  $\tau^+\tau^-b\bar{b}$  [9, 15–21]. Phenomenological studies about Higgs boson pair production and the feasibility of Higgs boson self-coupling measurements can be found e.g. in Refs. [22–47].

The leading order (one-loop) calculation of Higgs boson pair production in gluon fusion has been performed in Refs. [48–50]. NLO corrections were calculated in the  $m_t \rightarrow \infty$  limit, where the top quark degrees of freedom are integrated out, leading to point-like effective couplings of gluons to Higgs bosons (“Higgs Effective Field Theory”, HEFT). Top quark mass effects have been included in various approximations. Calculating the NLO corrections within the heavy top limit and then rescaling the result differentially by a factor  $B_{FT}/B_{HEFT}$ , where  $B_{FT}$  denotes the leading order matrix element squared in the full theory, is denoted “Born-improved HEFT” approximation. This calculation [51], implemented in the program HPAIR, led to a K-factor of about two. In Ref. [52], another approximation, called “FT<sub>approx</sub>”, was introduced, which contains the full top quark mass dependence in the real radiation, while the virtual part is calcu-

lated in the HEFT approximation and rescaled by the re-weighting factor  $B_{FT}/B_{HEFT}$ . The “FT’<sub>approx</sub>” result [52] in addition uses partial NLO results for the virtual part, i.e. it employs the exact results where they are known from single Higgs production. The “FT<sub>approx</sub>” calculation leads to a cross section which is about 10% smaller than the Born-improved NLO HEFT cross section. Using the “FT’<sub>approx</sub>” procedure, the reduction is about 9% with respect to the Born-improved NLO HEFT result. It was also found that top width effects can reach up to  $-4\%$  above the  $t\bar{t}$  threshold [52]. At LO, a finite top width reduces the total cross section at  $\sqrt{s} = 14$  TeV by about 2%. In our calculation we do not include a finite top width.

In addition, the HEFT results at NLO and NNLO have been improved by an expansion in  $1/m_t^{2\rho}$  in Refs. [53–56], with  $\rho^{\max} = 6$  at NLO, and  $\rho^{\max} = 2$  for the soft-virtual part at NNLO [55]. In the latter reference it is also demonstrated that the sign of the finite top mass corrections, amounting to about  $\pm 10\%$ , depends on whether the re-weighting factor is applied at differential level, i.e. before the integration over the partonic centre of mass energy, or at total cross section level.

The NNLO QCD corrections in the heavy top limit have been performed in Refs. [54, 57, 58], and they have been supplemented by an expansion in  $1/m_t^2$  in Ref. [55] and by resummation at NLO+NNLL in Ref. [59]. The most precise results within the infinite top mass approximation are NNLO+NNLL resummed results, calculated in Ref. [60], leading to K-factors of about 1.2 relative to the Born-improved HEFT result. Very recently, fully differential NNLO results in the HEFT approximation have become available [61].

As the different approximations partly led to corrections with opposite sign, there was a rather large uncertainty associated with the unknown effect of the exact top quark mass dependence at NLO, which was estimated to be of the order of 10% at  $\sqrt{s} = 14$  TeV. The full NLO calculation which became available recently [62], revealed a 14% reduction of the total cross section compared to the Born improved HEFT at  $\sqrt{s} = 14$  TeV and a 24% reduction at  $\sqrt{s} = 100$  TeV.

At differential distribution level, we found that the deviation from the Born-improved HEFT approximation can be as large as 50% in the tails of distributions like the Higgs boson pair invariant mass or Higgs boson transverse momentum distributions.

This paper is structured as follows. In Section 2 we give details of the calculation, in particular about the calculation of the two-loop amplitude and about the  $1/m_t$  expansion which we also performed. In Section 3 we discuss our phenomenological results. We study various distributions at  $\sqrt{s} = 14$  TeV and  $\sqrt{s} = 100$  TeV, comparing the full NLO result to different approximations. We also analyze the effects of non-Standard Model values of the triple Higgs coupling.

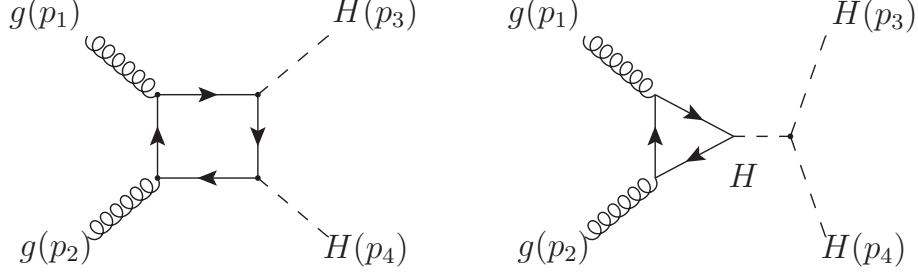


**Figure 1:** Diagrams contributing to the process  $gg \rightarrow hh$  at leading order.

## 2 Details of the calculation

### 2.1 Amplitude structure

The leading order diagrams contributing to the process  $gg \rightarrow hh$  are shown in Fig. 1. As the cross section does not have a tree level contribution, the virtual contribution at next-to-leading order involves two-loop diagrams, and the NLO real radiation part involves one-loop diagrams up to pentagons.

The amplitude for the process  $g(p_1, \mu) + g(p_2, \nu) \rightarrow h(p_3) + h(p_4)$  can be decomposed into form factors as

$$\begin{aligned} \mathcal{M}_{ab} &= \delta_{ab} \epsilon^\mu(p_1, n_1) \epsilon^\nu(p_2, n_2) \mathcal{M}_{\mu\nu} \\ \mathcal{M}^{\mu\nu} &= \frac{\alpha_s}{8\pi v^2} \{ F_1(\hat{s}, \hat{t}, m_h^2, m_t^2, D) T_1^{\mu\nu} + F_2(\hat{s}, \hat{t}, m_h^2, m_t^2, D) T_2^{\mu\nu} \} , \end{aligned} \quad (2.1)$$

where  $n_1, n_2$  are arbitrary reference momenta for the two gluon polarization vectors  $\epsilon^\mu, \epsilon^\nu$ . Colour indices are denoted by  $a, b$  and

$$\hat{s} = (p_1 + p_2)^2, \quad \hat{t} = (p_1 - p_3)^2, \quad \hat{u} = (p_2 - p_3)^2. \quad (2.2)$$

The decomposition into tensors carrying the Lorentz structure is not unique. It is however convenient to define the form factors such that [49]

$$\begin{aligned} \mathcal{M}^{++} &= \mathcal{M}^{--} = -\frac{\alpha_s}{8\pi v^2} F_1 \\ \mathcal{M}^{+-} &= \mathcal{M}^{-+} = -\frac{\alpha_s}{8\pi v^2} F_2 , \end{aligned} \quad (2.3)$$

which is fulfilled with the following definitions

$$\begin{aligned} T_1^{\mu\nu} &= g^{\mu\nu} - \frac{p_1^\nu p_2^\mu}{p_1 \cdot p_2} , \\ T_2^{\mu\nu} &= g^{\mu\nu} + \frac{1}{p_T^2 (p_1 \cdot p_2)} \{ m_h^2 p_1^\nu p_2^\mu - 2(p_1 \cdot p_3) p_3^\nu p_2^\mu - 2(p_2 \cdot p_3) p_3^\mu p_1^\nu + 2(p_1 \cdot p_2) p_3^\nu p_3^\mu \} \end{aligned} \quad (2.4)$$

where  $p_T^2 = (\hat{u} \hat{t} - m_h^4)/\hat{s}$ ,  $T_1 \cdot T_2 = D - 4$ ,  $T_1 \cdot T_1 = T_2 \cdot T_2 = D - 2$ .

At leading order, we can further split  $F_1$  into a “triangle” and a “box” contribution

$$F_1(\hat{s}, \hat{t}, m_h^2, m_t^2, D) = F_\Delta(\hat{s}, \hat{t}, m_h^2, m_t^2, D) + F_\square(\hat{s}, \hat{t}, m_h^2, m_t^2, D). \quad (2.5)$$

As the LO form factor  $F_\Delta$  only contains the triangle diagrams, which have no angular momentum dependence, it can be attributed entirely to an s-wave contribution. The form factors  $F_\square$  and  $F_2$  can be attributed to the spin-0 and spin-2 states of the scattering amplitude, respectively.

We can get an idea about the angular dependence of  $F_1$  and  $F_2$  by considering the partial wave decomposition of the scattering amplitude, which is independent of the loop order. It should be noted however that this analysis is valid for  $2 \rightarrow 2$  scattering. At NLO, the cross section for the process  $gg \rightarrow HH$  also contains a  $2 \rightarrow 3$  scattering contribution from the real radiation. Therefore the analysis of the angular dependence below does not apply to the full NLO cross section.

In general, for a scattering process  $a + b \rightarrow c + d$  with the corresponding helicities  $\lambda_a, \dots, \lambda_d$ , the partial wave decomposition reads [63–65]

$$\langle \theta \phi \lambda_c \lambda_d | T(E) | 00 \lambda_a \lambda_b \rangle = 16\pi \sum_J (2J+1) \langle \lambda_c, \lambda_d | T^J(E) | \lambda_a, \lambda_b \rangle e^{i(s_i - s_f)\phi} d_{s_i, s_f}^J(\theta), \quad (2.6)$$

with  $s_i = \lambda_a - \lambda_b$  and  $s_f = \lambda_c - \lambda_d$ , and where  $\langle \theta \phi \lambda_c \lambda_d | T(E) | 00 \lambda_a \lambda_b \rangle$  denotes the transition matrix element. Unitarity must hold for each partial wave independently, *i.e.*  $|T^J| \leq 1$ . Thus the amplitude is decomposed into (orthogonal) Wigner  $d$ -functions  $d_{s_i, s_f}^J(\theta)$ , where  $J$  denotes the total angular momentum and  $s_i, s_f$  the total spin of the initial and final state, respectively. The structure of the amplitude is such that  $F_1$  only contributes to  $s_i = 0$ , while  $F_2$  only contributes to  $s_i = 2$ .  $F_1$  can have both a component proportional to  $d_{0,0}^0(\theta)$  as well as one proportional to  $d_{0,0}^2(\theta)$ , while  $F_2$  is proportional to  $d_{2,0}^2(\theta)$ . The  $d$ -functions  $d_{0,0}^J(\theta)$  are proportional to the Legendre-Polynomials  $P_J(\cos \theta)$ . As  $P_0(x) = 1$ ,  $P_2(x) = \frac{1}{2}(3x^2 - 1)$  and  $d_{2,0}^2(\theta) \sim \sin^2 \theta$ , we can conclude that the angular dependence of  $F_2$  should be  $\sim \sin^2 \theta$ . From the analytic expression for  $F_2$  at leading order [49], we can verify that indeed  $F_2 \sim p_T^2 = (\hat{u} \hat{t} - m_h^4)/\hat{s} = \frac{\hat{s}}{4} \beta_h^2 \sin^2 \theta$  where  $\beta_h^2 = 1 - 4m_h^2/\hat{s}$ .

Further, it is known that the leading contributions to the amplitude come from the lower partial waves in Eq. (2.6). Therefore we also conclude that the contribution from  $F_2$  should be subleading with respect to  $F_1$  in most of the kinematic regions. Indeed we observe that the contribution of the form factor  $F_2$  to the virtual two-loop amplitude is suppressed as compared to  $F_1$ .

## 2.2 Leading Order cross section

The functions  $F_i$  at leading order with full mass dependence can be found e.g. in Refs. [49, 50]. At LO, the “triangle” form factor has the simple form

$$\begin{aligned} F_\Delta &= C_\Delta \bar{F}_\Delta, \quad C_\Delta = \frac{\lambda_{hhh}}{\hat{s} - m_h^2}, \quad \lambda_{hhh} = 3m_h^2 \lambda, \\ \bar{F}_\Delta &= 4m_q^2 \{2 + (4m_q^2 - \hat{s})C_0\} = 2\hat{s} \tau_q [1 + (1 - \tau_q)f(\tau_q)], \end{aligned} \quad (2.7)$$

where  $\lambda = 1$  in the Standard Model,  $\tau_q = 4m_q^2/\hat{s}$  and

$$\begin{aligned} f(\tau_q) &= \begin{cases} \arcsin^2 \frac{1}{\sqrt{\tau_q}} & \text{for } \tau_q \geq 1 \\ -\frac{1}{4} \left[ \log \frac{1+\sqrt{1-\tau_q}}{1-\sqrt{1-\tau_q}} - i\pi \right]^2 & \text{for } \tau_q < 1 \end{cases} \\ C_0 &= \int \frac{d^4 q}{i\pi^2} \frac{1}{(q^2 - m_q^2) [(q + p_1)^2 - m_q^2] [(q + p_1 + p_2)^2 - m_q^2]}. \end{aligned} \quad (2.8)$$

The partonic leading order cross section for  $gg \rightarrow hh$  can be written as

$$\hat{\sigma}^{\text{LO}}(gg \rightarrow hh) = \frac{\alpha_s^2(\mu_R)}{2^{12} v^4 (2\pi)^3 \hat{s}^2} \int_{\hat{t}_-}^{\hat{t}_+} d\hat{t} \{ |F_1|^2 + |F_2|^2 \}. \quad (2.9)$$

The integration limits  $\hat{t}^\pm$  are derived from a momentum parametrisation in the centre-of-mass frame, leading to  $\hat{t}_\pm = m_h^2 - \frac{\hat{s}}{2} (1 \mp \beta_h)$ , where  $\beta_h^2 = 1 - 4\frac{m_h^2}{\hat{s}}$ .

To obtain the hadronic cross section, we also have to integrate over the PDFs. Defining the luminosity function as

$$\frac{d\mathcal{L}_{ij}}{d\tau} = \sum_{ij} \int_\tau^1 \frac{dx}{x} f_i(x, \mu_F) f_j\left(\frac{\tau}{x}, \mu_F\right), \quad (2.10)$$

the total cross section reads

$$\sigma^{\text{LO}} = \int_{\tau_0}^1 d\tau \frac{d\mathcal{L}_{gg}}{d\tau} \hat{\sigma}^{\text{LO}}(\hat{s} = \tau s), \quad (2.11)$$

where  $s$  is the square of the hadronic centre of mass energy,  $\tau_0 = 4m_h^2/s$ , and  $\mu_F$  is the factorization scale.

### 2.2.1 Heavy top limit

In the  $m_t \rightarrow \infty$  approximation the LO form factors are given by

$$\bar{F}_\Delta \rightarrow \frac{4}{3}\hat{s}, \quad F_\square \rightarrow -\frac{4}{3}\hat{s}, \quad F_2 \rightarrow 0, \quad (2.12)$$

which implies for the the effective  $ggH$  and  $ggHH$  couplings  $c_h$  and  $c_{hh}$ <sup>1</sup>

$$c_h = -c_{hh} = -\frac{\alpha_s}{4\pi} \frac{i}{3} + \mathcal{O}\left(\frac{m_h^2}{4m_t^2}\right). \quad (2.13)$$

From the expressions above we can derive the following expression for the squared amplitude in the heavy top limit :

$$|\mathcal{M}|^2 \sim \frac{2}{9} - \frac{4}{3} m_h^2 \frac{\lambda}{\hat{s} - m_h^2} + 2 m_h^4 \frac{\lambda^2}{(\hat{s} - m_h^2)^2}. \quad (2.14)$$

For  $\lambda = 1$ , this expression vanishes at the Higgs boson pair production threshold  $\hat{s} \sim 4m_h^2$ . This explains why near the threshold the contributions containing the triple Higgs boson coupling and the ones which do not contain an s-channel Higgs boson exchange almost cancel. On the other hand, if the triple Higgs boson coupling was different from the Standard Model value, for example equal to zero, this should be clearly seen from the behaviour of the  $m_{hh}$  distribution. We investigate the effects of non-standard values for the triple Higgs boson coupling in Section 3.3.

## 2.3 NLO cross section

The NLO cross section is composed of various parts, which we discuss separately in the following.

$$\sigma^{\text{NLO}}(pp \rightarrow hh) = \sigma^{\text{LO}} + \sigma^{\text{virt}} + \sigma_{gg}^r + \sigma_{gq}^r + \sigma_{g\bar{q}}^r + \sigma_{q\bar{q}}^r. \quad (2.15)$$

The contributions from the real radiation,  $\sigma^r$ , can be divided into four channels, according to the partons in the initial state. The  $q\bar{q}$  channel is infrared finite. Details are given in Section 2.3.2.

---

<sup>1</sup>Higher order corrections to these effective couplings, and to couplings involving more than two Higgs bosons, can be found in Ref. [66] and references therein.



### 2.3.1 Calculation of the virtual two-loop amplitude

#### Amplitude generation

For the virtual two-loop amplitude, we use projectors  $P_j^{\mu\nu}$  to achieve a separation into objects carrying the Lorentz structure  $T_i^{\mu\nu}$  and the form factors  $F_1$  and  $F_2$ ,

$$P_1^{\mu\nu} \mathcal{M}_{\mu\nu} = \frac{\alpha_s}{8\pi v^2} F_1(\hat{s}, \hat{t}, m_h^2, m_t^2, D) ,$$

$$P_2^{\mu\nu} \mathcal{M}_{\mu\nu} = \frac{\alpha_s}{8\pi v^2} F_2(\hat{s}, \hat{t}, m_h^2, m_t^2, D) .$$

In  $D$  dimensions we can use the tensors  $T_i^{\mu\nu}$ , defined in Eqs. (2.4), to build the projectors

$$P_1^{\mu\nu} = \frac{1}{4} \frac{D-2}{D-3} T_1^{\mu\nu} - \frac{1}{4} \frac{D-4}{D-3} T_2^{\mu\nu} , \quad (2.16)$$

$$P_2^{\mu\nu} = -\frac{1}{4} \frac{D-4}{D-3} T_1^{\mu\nu} + \frac{1}{4} \frac{D-2}{D-3} T_2^{\mu\nu} . \quad (2.17)$$

The virtual amplitude has been generated with an extension of the program GOSAM [67, 68], where the diagrams are generated using QGRAF [69] and then further processed using FORM [70, 71]. The two-loop extension of GOSAM contains an automated python interface to REDUZE [72], which implies that the user has to provide the integral families when running GOSAM-2loop. The other input files needed by REDUZE are generated automatically by GOSAM-2loop, based on the kinematics of the given process. The reduction of the integrals occurring in the amplitude to master integrals should be performed separately, where in principle either of the codes REDUZE [72], FIRE5 [73] or LITERED [74] can be used. Examples of two-loop diagrams contributing to Higgs boson pair production are shown in Fig. 2.

We would like to point out again that the distinction between “triangle diagrams” and “box diagrams” becomes ambiguous beyond the leading order. At two-loop and beyond there are diagrams which contain triangle sub-diagrams but which do not contain the Higgs boson self coupling, see Fig. 2k.

#### Integral families and reduction

For the reduction of planar diagrams we have defined five integral families. Each family contains nine propagators which allows irreducible scalar products in the numerator to be written in terms of inverse propagators prior to reduction. We chose a non-minimal set of integral families in favour of preserving symmetries as much as possible. We find that integrals with up to four inverse propagators appear in the amplitude and must be reduced. The families are listed in Table 1.

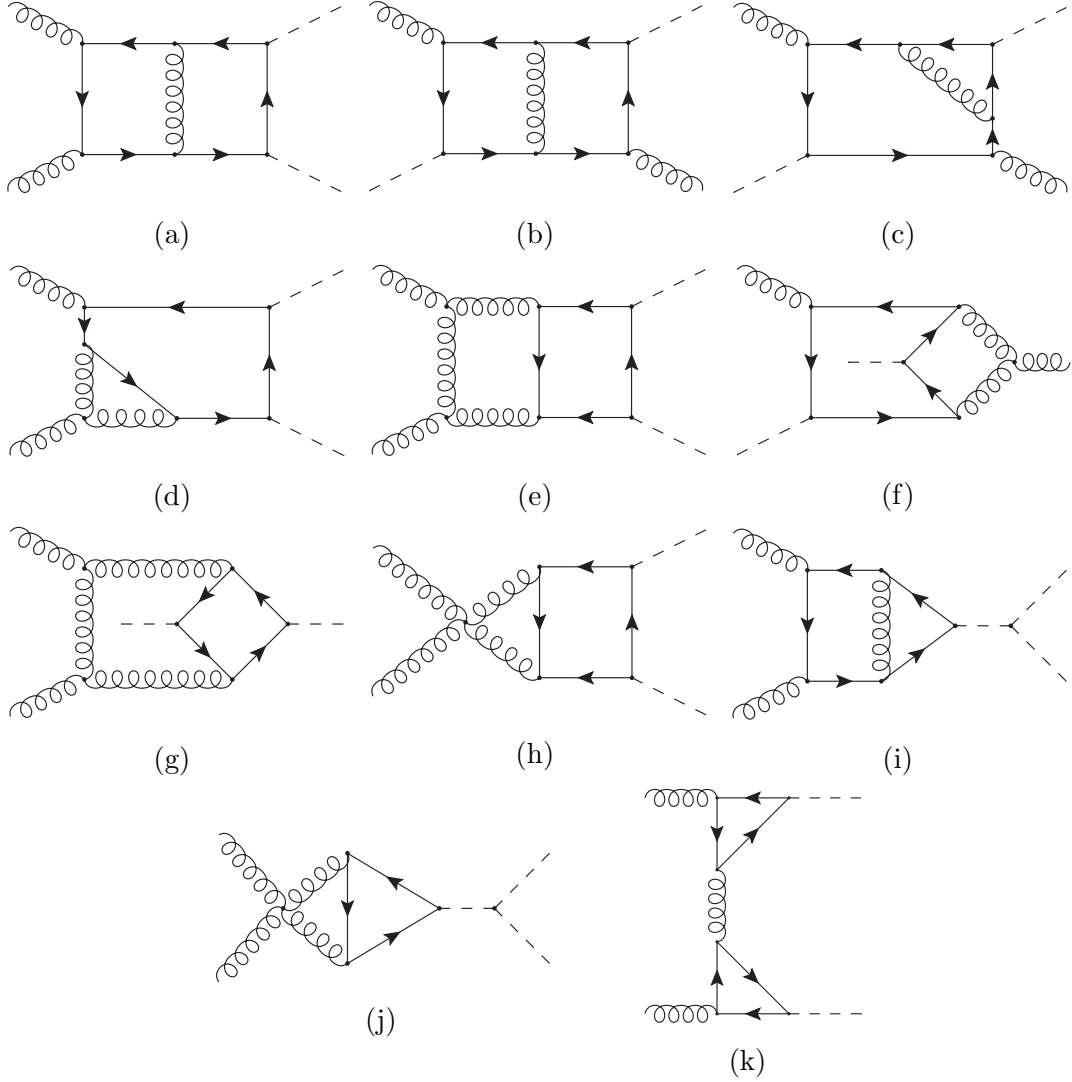


**Figure 2:** Examples of two-loop diagrams entering the virtual amplitude.

The amplitude generation leads to about 10000 integrals before any symmetries are taken into account. After accounting for symmetries and after reduction (complete reduction of the planar sectors and partial reduction of the non-planar ones), we end up with 145 planar master integrals plus 70 non-planar integrals, and a further 112 integrals that differ by a crossing. As these integrals contain four independent mass scales,  $\hat{s}, \hat{t}, m_t^2, m_h^2$ , only a small subset is known analytically. Besides the diagrams which are factorizing into two one-loop diagrams [56], the known integrals are the two-loop diagrams with two light-like legs and one massive leg, which enter single Higgs boson production, calculated e.g. in Refs. [75–79], and the triangles with one light-

$F_1$	$F_2$	$F_3$
$k_1^2 - m_t^2$	$k_1^2 - m_t^2$	$k_1^2$
$k_2^2 - m_t^2$	$k_2^2 - m_t^2$	$(k_1 - k_2)^2 - m_t^2$
$(k_1 - k_2)^2$	$(k_1 - k_2)^2$	$(k_1 + p_1)^2$
$(k_1 + p_1)^2 - m_t^2$	$(k_1 + p_1)^2 - m_t^2$	$(k_2 + p_1)^2 - m_t^2$
$(k_2 + p_1)^2 - m_t^2$	$(k_2 + p_1)^2 - m_t^2$	$(k_1 - p_2)^2$
$(k_1 - p_2)^2 - m_t^2$	$(k_1 - p_3)^2 - m_t^2$	$(k_2 - p_2)^2 - m_t^2$
$(k_2 - p_2)^2 - m_t^2$	$(k_2 - p_3)^2 - m_t^2$	$(k_2 - p_2 - p_3)^2 - m_t^2$
$(k_1 - p_2 - p_3)^2 - m_t^2$	$(k_1 - p_2 - p_3)^2 - m_t^2$	$(k_1 + p_1 + p_3)^2$
$(k_2 - p_2 - p_3)^2 - m_t^2$	$(k_2 - p_2 - p_3)^2 - m_t^2$	$(k_2 + p_1 - p_2)^2$
$F_4$	$F_5$	
$k_1^2 - m_t^2$	$k_1^2$	
$k_2^2$	$k_2^2 - m_t^2$	
$(k_1 - k_2)^2 - m_t^2$	$(k_1 - k_2)^2 - m_t^2$	
$(k_1 + p_1)^2 - m_t^2$	$(k_1 + p_1)^2$	
$(k_2 + p_1)^2$	$(k_2 + p_1)^2 - m_t^2$	
$(k_1 - p_2)^2 - m_t^2$	$(k_1 - p_3)^2$	
$(k_2 - p_2)^2$	$(k_2 - p_3)^2 - m_t^2$	
$(k_1 - p_2 - p_3)^2 - m_t^2$	$(k_1 - p_2 - p_3)^2$	
$(k_2 - p_2 - p_3)^2$	$(k_2 - p_2 - p_3)^2 - m_t^2$	

**Table 1:** Integral families for the reduction of the planar diagrams. The non-planar integrals were computed as tensor integrals, see text.

like and two off-shell legs occurring in the two-loop calculation of  $H \rightarrow Z\gamma$  [80, 81]. However, we calculate all integrals numerically using the program SECDEC [82–84].

As the integral basis is not unique, we choose to have two set-ups, relying on different sets of basis integrals. This serves as a strong check of the calculation of the virtual amplitude. It has previously been noted that using a finite basis [85] along with sector decomposition can increase the precision obtained by numerical integration for a given number of sampling points [86]. We also observed that switching to a finite basis in some of the planar sectors turned out to be beneficial for the numerical evaluation of the master integrals.

A complete reduction could not be obtained for the non-planar 4-point integrals. The inverse propagators appearing in unreduced integrals were rewritten in terms of scalar products such that the resulting integrals had the lowest possible tensor rank. The tensor integrals (up to rank 4) were then directly computed with SECDEC.

We would like to mention that non-planar diagrams also contribute to the leading colour coefficient. Therefore we could not identify a contribution which is both dominant and gauge invariant where only planar integrals contribute.

## Renormalization

We expand the amplitude in  $a_0 = \alpha_0/(4\pi)$ , where  $\alpha_0$  is the bare QCD coupling. The bare amplitude can be written as

$$\mathcal{A}_B = a_0 \mathcal{A}_B^{(1)} + a_0^2 \mathcal{A}_B^{(2)} + \mathcal{O}(a_0^3), \quad (2.18)$$

where the one- and two-loop coefficients are given by

$$\mathcal{A}_B^{(1)} = S_\epsilon \mu_0^{2\epsilon} \left[ \tilde{b}_0^{(1)} + \tilde{b}_1^{(1)} \epsilon + \tilde{b}_2^{(1)} \epsilon^2 + \mathcal{O}(\epsilon^3) \right], \quad (2.19)$$

$$\mathcal{A}_B^{(2)} = S_\epsilon^2 \mu_0^{4\epsilon} \left[ \frac{\tilde{b}_{-2}^{(2)}}{\epsilon^2} + \frac{\tilde{b}_{-1}^{(2)}}{\epsilon} + \tilde{b}_0^{(2)} + \mathcal{O}(\epsilon) \right]. \quad (2.20)$$

Here  $\mu_0^2$  is a parameter introduced in dimensional regularisation to maintain a dimensionless bare coupling and  $S_\epsilon = e^{-\gamma_E \epsilon} (4\pi)^\epsilon$ , with  $\gamma_E$  the Euler constant. The one-loop amplitude is expanded to  $\mathcal{O}(\epsilon^2)$  as it appears multiplied by the Catani-Seymour insertion operator stemming from the integrated dipoles,  $\mathbf{I}$ , which has poles of  $\mathcal{O}(\epsilon^{-2})$ .

To renormalize the gluon wave function we must multiply the amplitude by  $(Z_A)^{\frac{1}{2}}$  for each external gluon leg, where  $Z_A$  is the gluon field renormalization constant. We renormalize the QCD coupling using the relation

$$a_0 = a Z_a \left( \frac{\mu_R^2}{\mu_0^2} \right)^\epsilon, \quad a = \frac{\alpha_s}{4\pi} \quad (2.21)$$

where  $\alpha_s$  is the renormalized coupling and  $Z_a$  is the associated renormalization constant. Here  $\mu_R$  is the renormalization scale and the dependence of  $\alpha_s$  on  $\mu_R$  is implicit. The top mass is renormalized by relating the bare top mass  $m_{t_0}^2$  to the renormalized top mass  $m_t^2$  via

$$m_{t_0}^2 = m_t^2 + a \delta m_t^2. \quad (2.22)$$

In practice, we compute top mass counter-term diagrams, treating  $a \delta m_t^2$  as a counter-term insertion in top quark lines and renormalize the top Yukawa coupling using

$$y_{t_0} = \left( 1 + a \frac{\delta m_t^2}{m_t^2} \right) y_t. \quad (2.23)$$

No Higgs wave function or mass renormalization is required as we compute only QCD corrections.

In our calculation we use conventional dimensional regularization (CDR) with  $D = 4 - 2\epsilon$ . We renormalize the top mass in the on-shell scheme and the QCD coupling in the  $\overline{\text{MS}}$  five-flavour scheme ( $N_f = 5$ ) with the top quark loops in the gluon self-energy subtracted at zero momentum.

The one-loop renormalization constants are given to first order in  $a$  by<sup>2</sup>

$$Z_A = 1 + a \delta Z_A + \mathcal{O}(a^2), \quad (2.24)$$

$$Z_a = S_\epsilon^{-1} [1 + a \delta Z_a + \mathcal{O}(a^2)], \quad (2.25)$$

where

$$\begin{aligned} \delta Z_A &= \left( \frac{m_t^2}{\mu_R^2} \right)^{-\epsilon} \left( -\frac{4}{3\epsilon} T_R \right), \\ \delta Z_a &= -\frac{1}{\epsilon} \beta_0 + \delta Z_a^{\text{hq}}, \quad \beta_0 = \frac{11}{3} C_A - \frac{4}{3} T_R N_f^{\text{light}}, \\ \delta Z_a^{\text{hq}} &= \left( \frac{m_t^2}{\mu_R^2} \right)^{-\epsilon} \frac{4}{3\epsilon} T_R, \end{aligned} \quad (2.26)$$

and the mass counter-term in the on-shell scheme is given by

$$\delta m_t^2 = \left( \frac{m_t^2}{\mu_R^2} \right)^{-\epsilon} 2 m_t^2 C_F \left( -\frac{3}{\epsilon} - 4 \right) + \mathcal{O}(\epsilon). \quad (2.27)$$

The coefficients  $\tilde{b}_i$  in (2.19), (2.20) contain integrals  $I_{r,s}(\hat{s}, \hat{t}, m_h^2, m_t^2)$ , where  $r$  denotes the number of propagators in the denominator and  $s$  denotes the number of propagators in the numerator and therefore defines the tensor rank of the integral. The integrals have mass dimension  $[I_{r,s}] = D L - 2r + 2s$ , with  $L$  the number of loops. We may therefore factor a dimensionful parameter  $M$  out of each integral such that they depend only on dimensionless ratios

$$I_{r,s}(\hat{s}, \hat{t}, m_h^2, m_t^2) = (M^2)^{-L\epsilon} (M^2)^{2L-r+s} I_{r,s} \left( \frac{\hat{s}}{M^2}, \frac{\hat{t}}{M^2}, \frac{m_h^2}{M^2}, \frac{m_t^2}{M^2} \right). \quad (2.28)$$

---

<sup>2</sup>Note that  $Z_a$  corresponds to the renormalization factor of the coupling  $g_s$  *squared*, therefore it is twice the expression for  $Z_{g_s}$  found in the literature, see e.g. Eq. (3.4) of Ref. [87].

The renormalized amplitude may then be written as

$$\begin{aligned}\mathcal{A}^{\text{virt}} &= \prod_{n_g} Z_A^{\frac{1}{2}} \mathcal{A}_B (a_0 \rightarrow a Z_a (\mu_R^2/\mu_0^2)^\epsilon, m_{t_0}^2 \rightarrow m_t^2 + a \delta m_t^2) \\ &= a \mathcal{A}^{(1)} + a^2 \left( \frac{n_g}{2} \delta Z_A + \delta Z_a \right) \mathcal{A}^{(1)} + a^2 \delta m_t^2 \mathcal{A}^{ct,(1)} + a^2 \mathcal{A}^{(2)} + \mathcal{O}(a^3),\end{aligned}\quad (2.29)$$

$$\mathcal{A}^{(1)} = \left( \frac{\mu_R^2}{M^2} \right)^\epsilon \left[ b_0^{(1)} + b_1^{(1)} \epsilon + b_2^{(1)} \epsilon^2 + \mathcal{O}(\epsilon^3) \right], \quad (2.30)$$

$$\mathcal{A}^{ct,(1)} = \left( \frac{\mu_R^2}{M^2} \right)^\epsilon \left[ c_0^{(1)} + c_1^{(1)} \epsilon + \mathcal{O}(\epsilon^2) \right], \quad (2.31)$$

$$\mathcal{A}^{(2)} = \left( \frac{\mu_R^2}{M^2} \right)^{2\epsilon} \left[ \frac{b_{-2}^{(2)}}{\epsilon^2} + \frac{b_{-1}^{(2)}}{\epsilon} + b_0^{(2)} + \mathcal{O}(\epsilon) \right], \quad (2.32)$$

where

$$\tilde{b}^{(L)} = (M^2)^{-L\epsilon} b^{(L)}, \quad \tilde{c}^{(L)} = (M^2)^{-L\epsilon} c^{(L)}. \quad (2.33)$$

Since  $\delta m_t^2$  contains poles of  $\mathcal{O}(\epsilon^{-1})$  the coefficient  $c$  of the top mass counter-term must be expanded to  $\mathcal{O}(\epsilon)$ . It is obtained by the insertion of a mass counter-term into the heavy quark propagators,

$$\Pi_{ab}^{\delta m}(p) = \frac{i\delta_{ac}}{\not{p} - m} (-i\delta m) \frac{i\delta_{cb}}{\not{p} - m}, \quad (2.34)$$

where  $a, b, c$  are colour indices in the fundamental representation. Alternatively, the mass counter-term can be obtained by taking the derivative of the one-loop amplitude with respect to  $m$ .

The coefficients  $b$  and  $c$  in (2.29) are calculated numerically. We have extracted the dependence of the coefficients on the renormalization scale and introduced a dependence on a new scale,  $M$ , which we keep fixed in our numerics.

For the infrared singularities stemming from the unresolved real radiation, we use the Catani-Seymour subtraction scheme [88]. The infrared poles of the virtual amplitude are cancelled after combination with the  $\mathbf{I}$ -operator, which is given by

$$\mathbf{I}_{gg}(\epsilon) = \frac{\alpha_s}{2\pi} \frac{(4\pi)^\epsilon}{\Gamma(1-\epsilon)} \left( \frac{\mu_R^2}{\hat{s}} \right)^\epsilon \cdot 2 \cdot \left\{ \frac{C_A}{\epsilon^2} + \frac{\beta_0}{2\epsilon} - C_A \frac{\pi^2}{3} + \frac{\beta_0}{2} + K_g \right\}, \quad (2.35)$$

where  $K_g$  is also defined by the Catani-Seymour subtraction scheme [88]. Inserting the

I-operator into the Born amplitude leads to<sup>3</sup>

$$\begin{aligned}
\mathcal{A}^{\text{IR ct}} &= \frac{1}{2} \cdot \mathbf{I}_{gg}(\epsilon) \otimes \mathcal{A}^{(1)} \\
&= a^2 \left( \frac{\mu_R^2}{\hat{s}} \right)^\epsilon \left( \frac{\mu_R^2}{M^2} \right)^\epsilon \left( 1 - \epsilon^2 \frac{\pi^2}{12} \right) \left\{ \frac{2C_A}{\epsilon^2} + \frac{\beta_0}{\epsilon} - C_A \frac{2\pi^2}{3} + \beta_0 + 2K_g \right\} \\
&\quad \times \left[ b_0^{(1)} + b_1^{(1)}\epsilon + b_2^{(1)}\epsilon^2 \right], \tag{2.36}
\end{aligned}$$

where we again have extracted a factor  $(M^2)^{-\epsilon}$  from the integrals contained in the one-loop amplitude. Using (2.29) and (2.36) we therefore have

$$\begin{aligned}
\mathcal{A}^{\text{virt}} + \mathcal{A}^{\text{IR ct}} &= a\mathcal{A}^{(1)} + a^2 \left( \frac{\mu_R^2}{M^2} \right)^\epsilon \left\{ \delta m_t^2 \left[ c_0^{(1)} + c_1^{(1)}\epsilon \right] + \left( \frac{\mu_R^2}{M^2} \right)^\epsilon \left[ \frac{b_{-2}^{(2)}}{\epsilon^2} + \frac{b_{-1}^{(2)}}{\epsilon} + b_0^{(2)} \right] \right. \\
&\quad \left. + \left[ b_0^{(1)} + b_1^{(1)}\epsilon + b_2^{(1)}\epsilon^2 \right] \left[ \left( \frac{\mu_R^2}{\hat{s}} \right)^\epsilon \left\{ \frac{2C_A}{\epsilon^2} + \frac{\beta_0}{\epsilon} + \text{fin.} \right\} - \frac{\beta_0}{\epsilon} \right] \right\} \\
&= a\mathcal{A}^{(1)} + a^2 \left( \frac{\mu_R^2}{M^2} \right)^\epsilon \left\{ \frac{1}{\epsilon^2} \left[ 2C_A b_0^{(1)} + b_{-2}^{(2)} \right] \right. \\
&\quad + \frac{1}{\epsilon} \left[ 2C_A b_0^{(1)} \ln \left( \frac{\mu_R^2}{\hat{s}} \right) + b_{-2}^{(2)} \ln \left( \frac{\mu_R^2}{M^2} \right) + b_{-1}^{(2)} - 6m_t^2 C_F c_0^{(1)} + 2C_A b_1^{(1)} \right] \\
&\quad + b_0^{(1)} \beta_0 \ln \left( \frac{\mu_R^2}{\hat{s}} \right) + \ln \left( \frac{\mu_R^2}{M^2} \right) b_{-1}^{(2)} - \ln \left( \frac{\mu_R^2}{m_t^2} \right) 6m_t^2 C_F c_0^{(1)} + 2C_A b_1^{(1)} \ln \left( \frac{\mu_R^2}{\hat{s}} \right) \\
&\quad + C_A b_0^{(1)} \ln^2 \left( \frac{\mu_R^2}{\hat{s}} \right) + \frac{b_{-2}^{(2)}}{2} \ln^2 \left( \frac{\mu_R^2}{M^2} \right) \\
&\quad \left. + \text{finite non-logarithmic terms} \right\}. \tag{2.37}
\end{aligned}$$

By construction the double pole in  $\epsilon$  must vanish, thus (2.37) implies

$$b_{-2}^{(2)} = -2C_A b_0^{(1)}. \tag{2.38}$$

Substituting the above relation back into (2.37) we see that the dependence on the renormalization scale  $\mu_R$  cancels in the single pole term. The dependence of the cross

---

<sup>3</sup> The factor of  $\frac{1}{2}$  is necessary to cancel the factor of 2 obtained from squaring  $\mathcal{A}^{\text{virt}} + \mathcal{A}^{\text{IR ct}}$  to get the cross section.

section on the factorization scale is encoded in the  $\mathbf{P}$  and  $\mathbf{K}$  terms of the Catani-Seymour framework [88].

### Integration of the two-loop amplitude

To evaluate the two-loop integrals appearing in the amplitude we first apply sector decomposition as implemented in SECDEC. In the Euclidean region sector decomposition resolves singularities in the regulator  $\epsilon$ , leaving only finite integrals over the Feynman parameters which can be evaluated numerically. In the physical region we treat the integrable singularities by contour deformation [83, 89–91]. To obtain the differential cross section we have to evaluate integrals at phase space points very close to threshold, where no special treatment was necessary but numerical convergence was considerably harder to achieve.

After sector decomposition each loop-integral  $I_j$  can be written as a sum over sectors  $s$  which have a Laurent series starting at some  $\epsilon$ -order  $e_s^{\min}$

$$I_j(\epsilon) = \sum_s \sum_{e > e_s^{\min}} \epsilon^e I_{j,s,e}. \quad (2.39)$$

For the numerical evaluation of the amplitude we structured the code such that the integrand of each sector-decomposed loop integral  $I_{j,s,e}$  is stored along with the Laurent series of their coefficients  $a_j$  appearing in the expressions for the amplitudes (2.30)–(2.32). E.g. at two-loop we write the amplitude as

$$\mathcal{A}^{(2)} = \left( \frac{\mu_R^2}{M^2} \right)^{2\epsilon} \sum_{j,s,e} I_{j,s,e} \cdot a_j(\epsilon) \quad (2.40)$$

and store  $a_j$  as a vector containing the coefficients of  $I_j$  in the expressions for  $b_k^{(2)}$ , leading to the amplitude structure given in Eq. (2.32).

Structuring the code this way allows us to dynamically set the number of sampling points used for each integral according to its contribution to the amplitude. After calculating each integral with a fixed number of sampling points, we assume that the integration error  $\Delta_j$  of the integrals scales as  $\Delta_j \propto t_j^{-\alpha}$  with the integration time  $t_j$ . To efficiently calculate the results  $b_k^{(i)}$  with a given relative accuracy  $\varepsilon_k^{(i)} = \Delta_k^{(i)}/b_k^{(i)}$ , we estimate the required number of sampling points for each integral such that the total time

$$T_k^{(i)} = \sum_j t_j + \bar{\lambda} \left( (\Delta_k^{(i)})^2 - \sum_j (\Delta_{j,k}^{(i)})^2 \right) \quad (2.41)$$



is minimal.  $\Delta_{j,k}^{(i)}$  is the error estimate of integral  $I_j$  including its coefficients in  $b_k^{(i)}$  and  $\bar{\lambda}$  is a Lagrange multiplier. Since the loop integrals can contribute to several results  $b_k^{(i)}$ , we apply the above optimization formula for each required order in  $\epsilon$  and for both form factors. For each integral, we then use the maximum of the estimated number of required sampling points. Instead of directly evaluating each integral with the calculated number of sampling points, we limit the number of new sampling points and iterate this procedure to reach the desired accuracy, updating the estimated number of sampling points after each iteration. The desired accuracy for the finite part of the two-loop amplitude ( $\varepsilon_0^{(2)}$ ) is set to 3% for form factor  $F_1$  and (depending on the ratio  $F_2/F_1$ ) to a value of 5-20% for form factor  $F_2$ .

For the integration we use a quasi-Monte Carlo method based on a rank-one lattice rule [92–94]. For suitable integrands, this rule provides a convergence rate of  $\mathcal{O}(1/n)$  as opposed to Monte Carlo or adaptive Monte Carlo techniques, such as VEGAS [95], which converge  $\mathcal{O}(1/\sqrt{n})$ , where  $n$  is the number of sampling points. While we observe a convergence rate of  $\mathcal{O}(1/n)$  for most of the integrals, the convergence of some integrals is worse and we therefore assume a scaling of  $\Delta_j(t_j)$  with exponent  $\alpha = 0.7$  when estimating the number of required sampling points.

The integration rule is implemented in OPENCL 1.1 and a further (OPENMP threaded) C++ implementation is used as a partial cross-check. The 913 phase-space points at 14 TeV (1029 phase-space points at 100 TeV) used for the current publication were computed with  $\sim 16$  dual NVIDIA TESLA K20X GPGPU nodes. More details on the numeric evaluation of the amplitudes can be found in Refs. [96, 97].

### 2.3.2 Real radiation

As we calculate a process which is loop-induced, the NLO corrections involve two-loop integrals. But, for the real part only single-unresolved radiation can occur. This means that a standard NLO infrared subtraction scheme can be used. We use the Catani-Seymour dipole formalism [88], combined with a phase space restriction parameter  $\alpha$  to restrict the dipole subtraction to a limited region, as suggested in Ref. [98].

There are four partonic channels for the real radiation contribution to the cross section:

$$\sigma^r(gg \rightarrow hh + g), \sigma^r(gq \rightarrow hh + q), \sigma^r(g\bar{q} \rightarrow hh + \bar{q}), \sigma^r(q\bar{q} \rightarrow hh + g) . \quad (2.42)$$

Including all crossings, there are 78 real radiation diagrams. Infrared singularities only originate from initial state radiation, diagrams with extra gluons radiated from a heavy quark line are infrared finite, which implies that the  $q\bar{q}$  channel is finite. Example diagrams are depicted in Fig. 3.

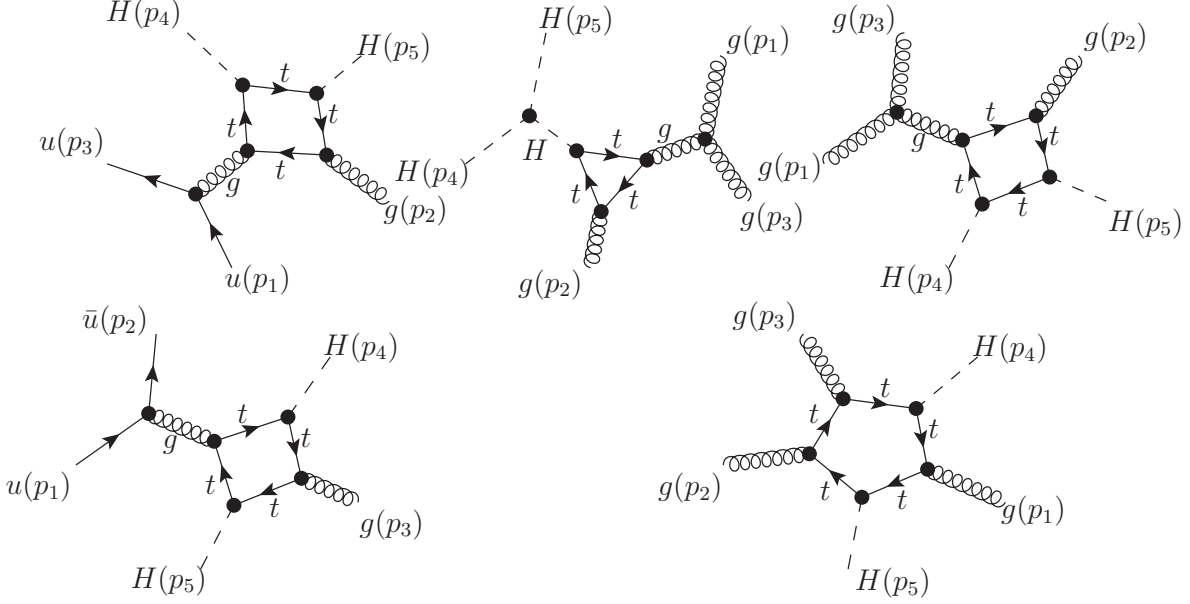


**Figure 3:** Examples of diagrams contributing to the real radiation part at NLO. The diagrams in the second row do not lead to infrared singularities.

## 2.4 Validation of the calculation and expansion in $1/m_t$

### 2.4.1 Expansion in $1/m_t^2$

We have calculated top mass corrections as an expansion in  $1/m_t^2$  in the following way: we write the partonic differential cross section as

$$d\hat{\sigma}_{\text{exp},N} = \sum_{\rho=0}^N d\hat{\sigma}^{(\rho)} \left( \frac{\Lambda}{m_t} \right)^{2\rho}, \quad (2.43)$$

where  $\Lambda \in \{\sqrt{\hat{s}}, \sqrt{\hat{t}}, \sqrt{\hat{u}}, m_h\}$ , and determine the first few terms (up to  $N = 3$ ) of this asymptotic series. The case  $N = 0$  reproduces to the usual effective theory approach, without the need to calculate Wilson coefficients separately, however.

To generate the diagrams we again use QGRAF [69]. The generation and expansion of the amplitude in small external momenta is then performed using Q2E/EXP [99, 100] and leads to two-loop vacuum integrals inserted into tree-level diagrams as well as one-loop vacuum integrals inserted into massless one-loop triangles. Whereas the vacuum integrals are evaluated with MATAD [101], the massless integrals can be expressed in terms of a single one-loop bubble, which we achieve with the help of REDUZE [72]. Again, the algebraic processing of the amplitude is done with FORM [70, 71].

The exact and expanded matrix elements were combined in the following way: a series expansion for the virtual corrections was performed then rescaled with the exact born,

$$\begin{aligned}
d\sigma^V + d\sigma^{LO}(\epsilon) \otimes \mathbf{I} &\approx d\sigma_{\text{exp},N}^V \frac{d\sigma^{LO}(\epsilon)}{d\sigma_{\text{exp},N}^{LO}(\epsilon)} + d\sigma^{LO}(\epsilon) \otimes \mathbf{I} \\
&= (d\sigma_{\text{exp},N}^V + d\sigma_{\text{exp},N}^{LO}(\epsilon) \otimes \mathbf{I}) \frac{d\sigma^{LO}(\epsilon)}{d\sigma_{\text{exp},N}^{LO}(\epsilon)} \\
&= \underbrace{(d\sigma_{\text{exp},N}^V + d\sigma_{\text{exp},N}^{LO}(\epsilon) \otimes \mathbf{I})}_{\equiv V_N} \frac{d\sigma^{LO}(\epsilon=0)}{d\sigma_{\text{exp},N}^{LO}(\epsilon=0)} + \mathcal{O}(\epsilon). \quad (2.44)
\end{aligned}$$

The first identity is valid because the colour structure of the exact and the expanded LO cross section are identical, and the second because the sum in the bracket is finite. Thus one needs to know only the  $\epsilon$  dependence of the expanded LO cross section in this approximation.

There is some ambiguity when to do the rescaling, i.e. before or after the phase-space integration, and convolution with the PDFs. We opt to do it on a fully differential level, i.e. the rescaling is done for each phase-space point individually.

#### 2.4.2 Checks of the calculation

We have verified for all calculated phase space points that the coefficients of the poles in  $\epsilon$  are zero within the numerical uncertainties. For a randomly chosen sample of phase-space points we have calculated the pole coefficients with higher accuracy and obtained a median cancellation of five digits.

Our implementation of the virtual two-loop amplitude has been checked to be invariant under the interchange of  $\hat{t}$  and  $\hat{u}$  at various randomly selected phase-space points. Single Higgs boson production has been re-calculated with the same setup for the virtual corrections and compared to the results obtained with the program SUSHI [102]. Further, the one-loop amplitude has been computed using an identical framework to the two-loop amplitude and has been checked against the result of Ref. [49].

As a further cross-check we have also calculated top mass corrections as an expansion in  $1/m_t^2$  as explained above. We have also compared to results provided to us by Jens Hoff for the orders  $N = 4, 5, 6$  in the expansion above, worked out in [55]. The result of the comparison is shown in Fig. 4. One can see that below the  $2m_t$  threshold, where agreement is to be expected, the expansion converges towards the full result.

The computation of the mass counter-term diagrams has been cross-checked by ex-

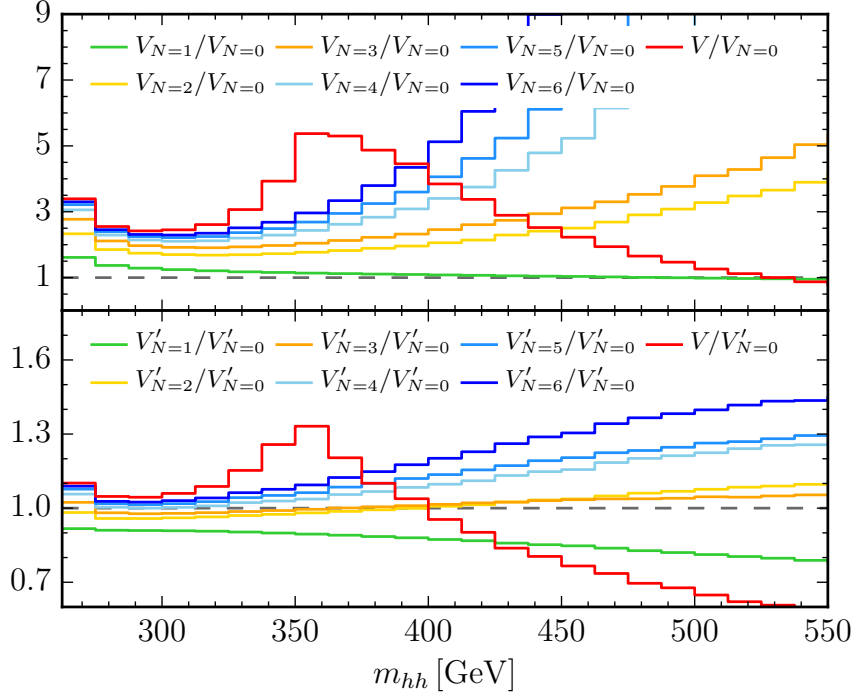


**Figure 4:** Comparison of the virtual part as defined in Eq. (2.44) with full top-quark mass dependence to various orders in a  $1/m_t^2$  expansion.  $V'_N$  denotes the Born-improved HEFT result to order  $N$  in the  $1/m_t^2$  expansion, i.e.  $V'_N = V_N B_{FT}/B_N$ . The results for the orders  $N = 4, 5, 6$  have been provided to us by Jens Hoff [55].

panding the one-loop amplitude about the bare top mass

$$\begin{aligned}
\mathcal{A}_B^{(1)}(m_t^2) &= \mathcal{A}_B^{(1)}(m_{t_0}^2) - a\delta m_t^2 \left( \frac{\partial}{\partial m_t^2} \mathcal{A}_B^{(1)}(m_t^2) \right) \Big|_{m_{t_0}^2} \\
&= \mathcal{A}_B^{(1)}(m_{t_0}^2) - a\delta m_t^2 \mathcal{A}_B^{ct,(1)}(m_{t_0}^2),
\end{aligned} \tag{2.45}$$

where  $\mathcal{A}^{ct,(1)}$  is the one-loop top quark mass counter-term.

On the real radiation side, we have verified the independence of the amplitude from the phase space restriction parameter  $\alpha$ . We have also varied the technical cut  $p_T^{\min}$  in the range  $10^{-2} \leq p_T^{\min}/\sqrt{s} \leq 10^{-6}$  to verify that the contribution to the total cross section is stable and independent of the cut within the numerical accuracy.

Further, we have compared to the results of Ref. [52] for the Born-improved HEFT and  $FT_{approx}$  approximations and found agreement within the numerical uncertainties [103].

$\sqrt{s}$	LO	B-i. NLO HEFT	NLO FT <sub>approx</sub>	NLO
14 TeV	19.85 <sup>+27.6%</sup> <sub>-20.5%</sub>	38.32 <sup>+18.1%</sup> <sub>-14.9%</sub>	34.26 <sup>+14.7%</sup> <sub>-13.2%</sub>	32.91 <sup>+13.6%</sup> <sub>-12.6%</sub>
100 TeV	731.3 <sup>+20.9%</sup> <sub>-15.9%</sub>	1511 <sup>+16.0%</sup> <sub>-13.0%</sub>	1220 <sup>+11.9%</sup> <sub>-10.7%</sub>	1149 <sup>+10.8%</sup> <sub>-10.0%</sub>

**Table 2:** Total cross sections at various centre of mass energies (in femtobarns). The uncertainty in percent is from 7-point scale variations as explained in the text. The central scale is  $m_{hh}/2$ . We used  $m_t = 173$  GeV,  $m_h = 125$  GeV. The PDF set is PDF4LHC15\_nlo\_100\_pdfas.

### 3 Phenomenological results

#### 3.1 Setup and total cross sections

We use the PDF4LHC15\_nlo\_100\_pdfas [104–107] parton distribution functions, along with the corresponding value for  $\alpha_s$  for both the NLO and the LO calculation. The masses have been set to  $m_h = 125$  GeV,  $m_t = 173$  GeV, and the top quark width has been set to zero. We use no cuts except a technical cut in the real radiation of  $p_T^{\min} = 10^{-4} \sqrt{\hat{s}}$ . The scale variation bands are the result of a 7-point scale variation [103] around the central scale  $\mu_0 = m_{hh}/2$ , with  $\mu_{R,F} = c_{R,F} \mu_0$ , where  $c_R, c_F \in \{2, 1, 0.5\}$ , except that the extreme variations  $(c_R, c_F) = (2, 0.5)$  and  $(c_R, c_F) = (0.5, 2)$  are omitted. The values we obtain for the total cross sections are shown in Table 2. The full NLO result has a statistical uncertainty of 0.3% at 14 TeV (0.16% at 100 TeV) stemming from the phase space integration and an additional uncertainty stemming from the numerical integration of the virtual amplitude of 0.04% at 14 TeV and 0.2% at 100 TeV. These uncertainties are not included in Table 2, where only scale variation uncertainties are shown.

#### 3.2 NLO distributions

In this section we show differential distributions at  $\sqrt{s} = 14$  TeV and  $\sqrt{s} = 100$  TeV for various observables and compare to the approximate results in order to assess the effect of the full top quark mass dependence at NLO. Results which are obtained within the effective field theory approach without reweighting by the leading order results in the full theory are always denoted by “basic HEFT”, while “B-i. NLO HEFT” stands for the Born-improved NLO HEFT result, where the NLO corrections have been calculated in the  $m_t \rightarrow \infty$  limit and then a reweighting factor  $B_{FT}/B_{HEFT}$  is applied (on differential level,  $B_{FT}$  stands for the Born amplitude squared in the full theory).

We decided to take the same bin sizes as in Ref. [61], such that the differences to the effective theory results can be exhibited most clearly. In Fig. 5 we show the Higgs

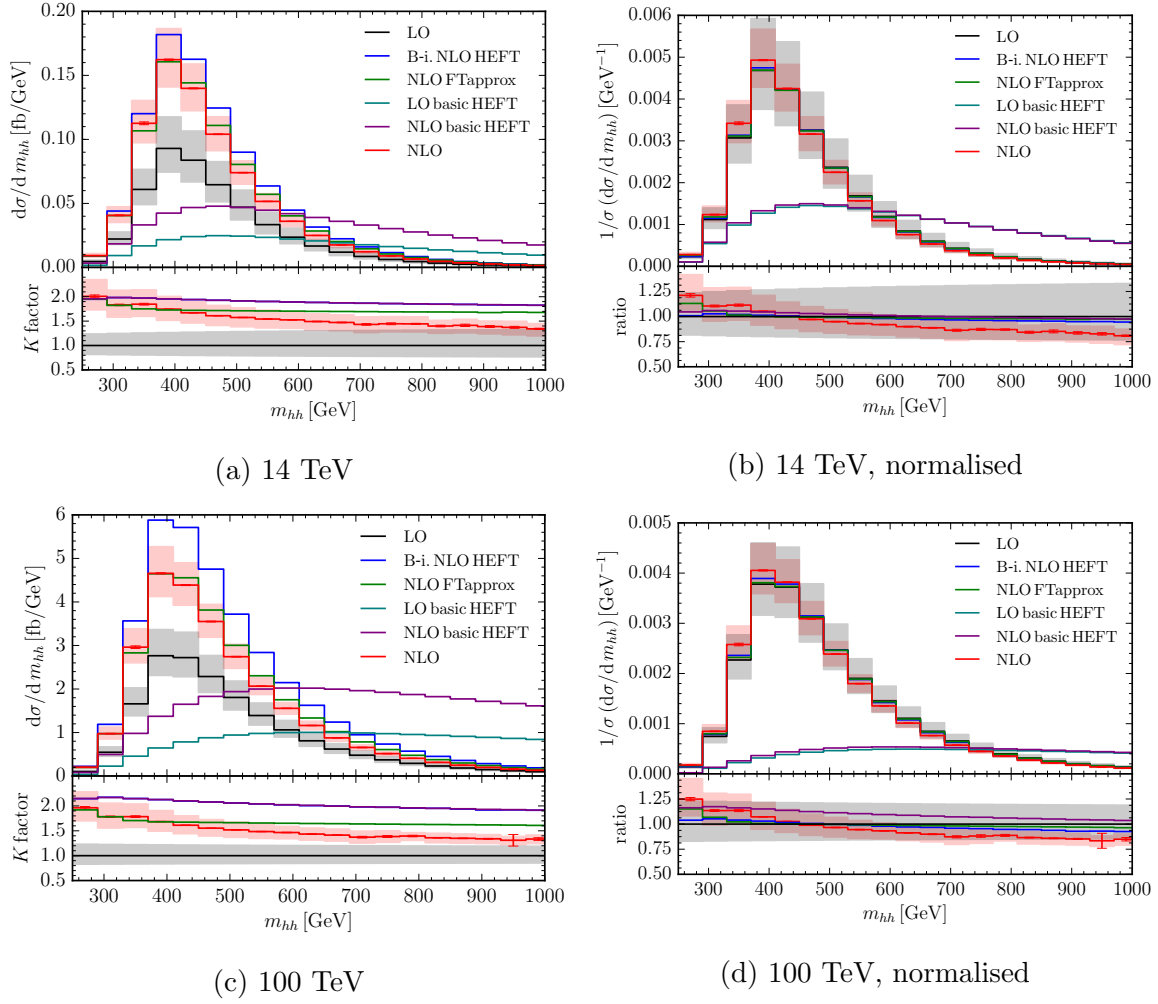


**Figure 5:** Higgs boson pair invariant mass distribution  $m_{hh}$  at  $\sqrt{s} = 14$  TeV and  $\sqrt{s} = 100$  TeV for absolute values (left panels) and normalised to the corresponding total cross section (right panels).

boson pair invariant mass distribution  $m_{hh}$  at  $\sqrt{s} = 14$  TeV and  $\sqrt{s} = 100$  TeV, comparing the full NLO result to various approximations. In particular, we compare to the “basic HEFT” approximation at  $\sqrt{s} = 14$  TeV, showing that it fails to describe the distribution. Comparing the results at 14 TeV and 100 TeV, we observe that the differences of the full NLO result to the Born-improved HEFT and also to the  $\text{FT}_{approx}$  result are amplified at 100 TeV, as expected, as the HEFT approximation does not have the correct high energy behaviour. This scaling behaviour will be discussed more in detail below. We also see that the K-factor is far from being uniform for the  $m_{hh}$  distribution, while the “basic HEFT” results suggest a uniform K-factor.

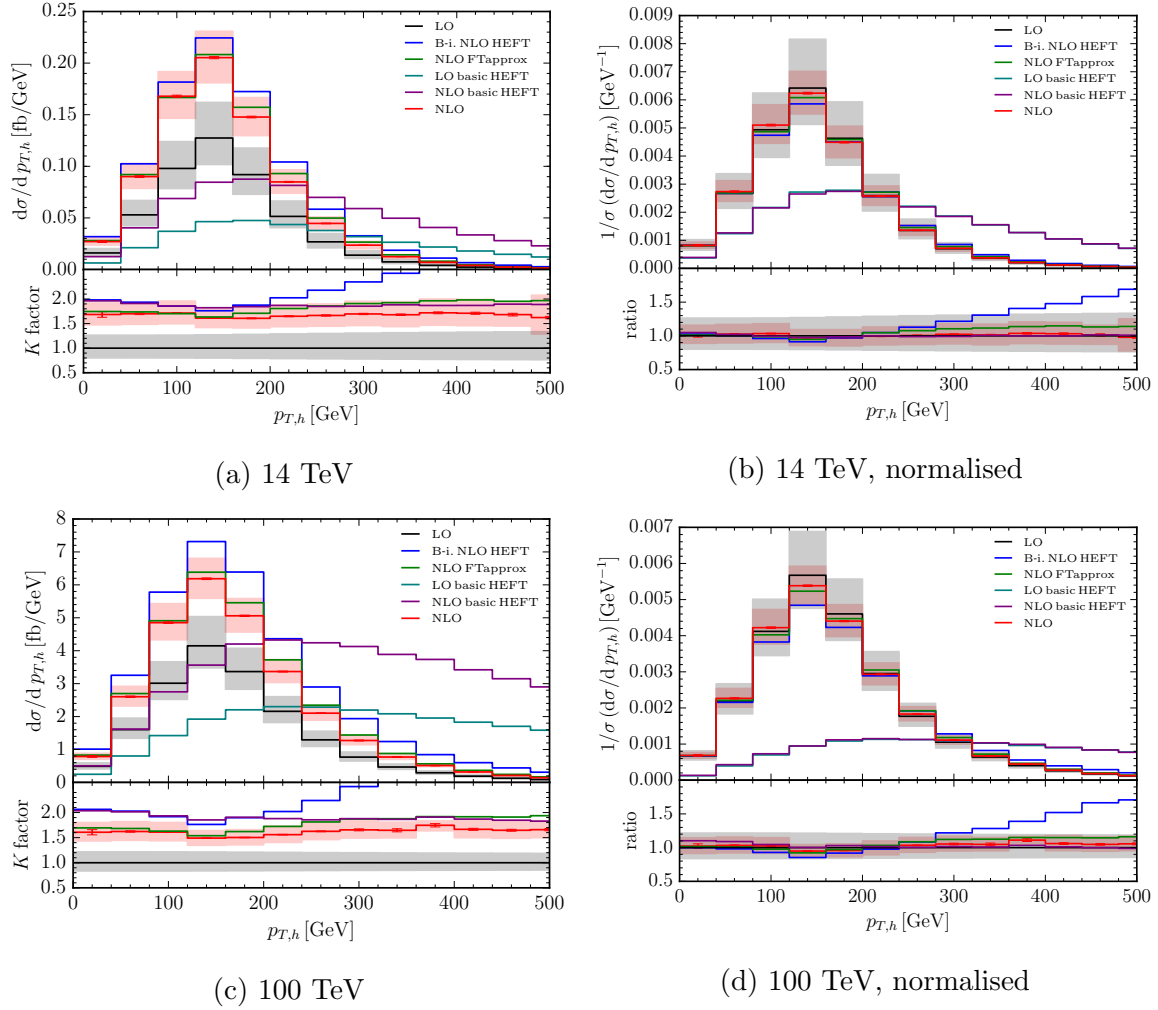


**Figure 6:** Transverse momentum distribution of (any) Higgs boson at  $\sqrt{s} = 14$  TeV and  $\sqrt{s} = 100$  TeV.

The  $p_{T,h}$  distribution shown in Fig. 6 denotes the distribution of the “single inclusive” Higgs boson transverse momentum, which denotes the transverse momentum distribution of any (randomly picked) Higgs boson. In contrast, Fig. 7 shows the transverse momentum distributions of the leading- $p_T$  (“harder”) and subleading- $p_T$  (“softer”) Higgs boson. It again becomes very clear that reweighting the basic HEFT result is indispensable in order to get at least somewhat close to the shape of the full NLO result. The  $p_{T,h}$  distribution in Fig. 6a shows that, while the Born-improved NLO HEFT result starts moving out of the scale variation band of the full NLO result at 14 TeV beyond  $p_{T,h} \sim m_t$ , the  $\text{FT}_{\text{approx}}$  result stays within the scale uncertainty band of the full NLO result, (even though it is clear that it systematically overestimates the full result by

about 20-30%). This is not surprising, as the tail of the  $p_{T,h}$  distribution is to a large extent dominated by the real radiation contribution. At  $\sqrt{s} = 100$  TeV, the  $\text{FT}_{approx}$  result leaves the scale variation band of the full NLO result beyond  $p_{T,h} \sim 280$  GeV, but still is much closer to the full result than the Born-improved NLO HEFT result. The differences of the latter to the full result are amplified at 100 TeV.

In any case, it is clear that the scale variation bands can only be indicative of missing higher order corrections in perturbation theory, while the top quark mass effects (or the omission of the exact top quark mass dependence) are in a different category. Therefore one cannot expect that, for example, the NLO HEFT scale variation band would comprise the full NLO result. It is also worth mentioning that the “ $\text{FT}'_{approx}$ ” approximation [52], where the partial two-loop results (known from single Higgs production) were included, turned out to be a worse approximation than “ $\text{FT}_{approx}$ ”, where the virtual part is given by the Born-improved NLO HEFT result, as it lead to a larger cross section than the “ $\text{FT}_{approx}$ ” one, and the latter is still larger than the full result. Note that for  $2 \rightarrow 2$  scattering the transverse momentum of the Higgs boson is given by  $p_T^2 = \frac{\hat{s}}{4} \beta_h^2 \sin^2 \theta$ . Therefore, at leading order, the  $p_{T,h}$  transverse momentum distribution directly reflects the angular dependence of the virtual amplitude. However, at NLO, the angular dependence of the form factors is influenced to a large extent by the real radiation. This can be seen from the distributions of the leading- $p_T$  (“harder”) and subleading- $p_T$  (“softer”) Higgs bosons shown in Fig. 7. The Higgs boson will pick up a large transverse momentum if it recoils against a hard jet, therefore the K-factor of the  $p_{T,h}^{\text{hard}}$  grows in the tail of the distribution, which is dominated by  $2 \rightarrow 3$  kinematics.

Fig. 8 shows the rapidity distributions of both the Higgs boson pair and the leading- $p_T$  Higgs boson. As the mass effects are uniformly distributed over the whole rapidity range, the K-factors are close to uniform for these distributions, and the  $\text{FT}_{approx}$  result is within 10% of the full result. In Fig. 9 we display the tails of the  $m_{hh}$  and  $p_{T,h}$  distributions on a logarithmic scale, in order to exhibit the scaling behaviour in the high energy limit. Using leading-log high energy resummation techniques, it can be shown [108] that at high transverse momentum, the differential partonic cross section for single Higgs (+jets) production  $d\sigma/dp_{T,h} \sim 1/p_{T,h}^a$  scales with  $a = 2$  in the full theory, however with  $a = 1$  in the effective theory. This behaviour also has been recently confirmed by a (leading order) calculation of Higgs + 1,2,3 jet production with full mass dependence [109]. In order to investigate the high energy scaling behaviour we fitted a line to the tail of the leading order  $m_{hh}$  distribution (with the luminosity factor set to one, plotted logarithmically), and found the following scaling behaviour: with full mass dependence, the scaling is as  $m_{hh}^{-3}$  for  $d\hat{\sigma}/dm_{hh}$  i.e. the partonic cross section scales as  $\hat{s}^{-1}$ , while in the basic HEFT approximation the scaling is as  $m_{hh}$  for  $d\hat{\sigma}/dm_{hh}$  i.e. the partonic cross section grows as  $\hat{s}$ . From Fig. 9 one can see that this



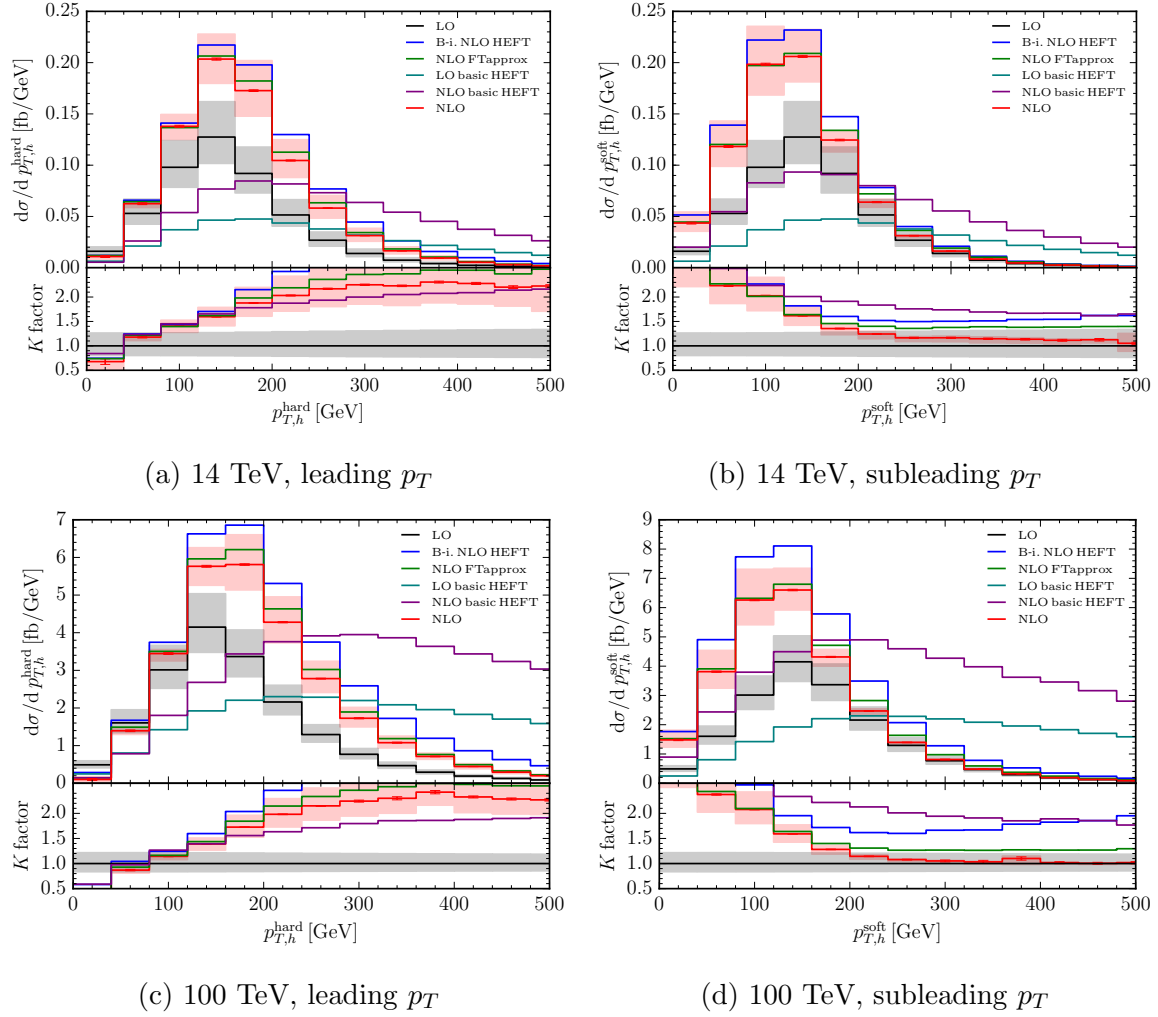
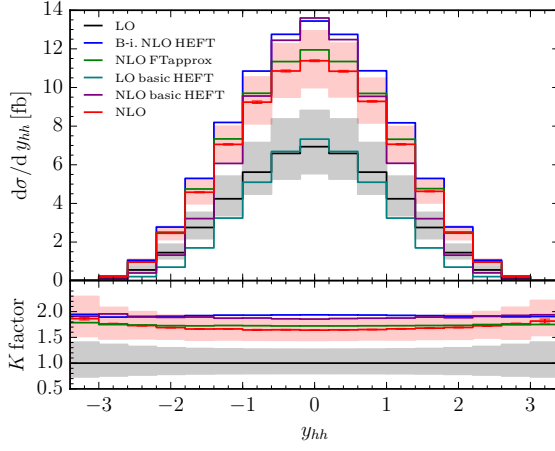


**Figure 7:** Transverse momentum distribution of the leading- $p_T$  Higgs boson (left panels) and the subleading- $p_T$  Higgs boson (right panels) at  $\sqrt{s} = 14$  TeV and  $\sqrt{s} = 100$  TeV.

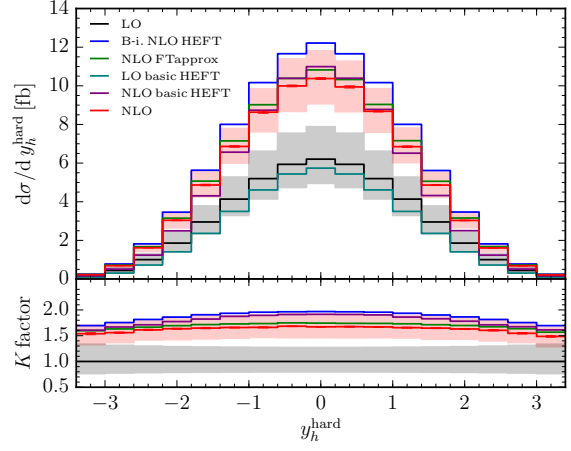
relative difference in the high-energy scaling behaviour between the full calculation and the basic HEFT approximation is similar at NLO.

In Fig. 10 we show distributions for an improved  $\text{FT}_{\text{approx}}$ , which is supplemented with higher order terms in the expansion of the virtual amplitude in  $1/m_t^2$  as given by Eq. (2.44), dubbed “exp. virt.” for “expanded virtuals”. We see a trend similar to the one for the virtual (plus  $\mathbf{I}$ -operator) part shown in Fig. 4.

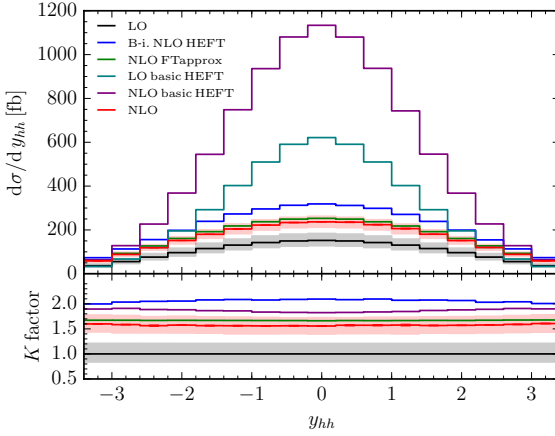
In order to better account for missing higher order corrections it is desirable to combine the full NLO with NNLO results obtained in the HEFT, ideally on a differential level.



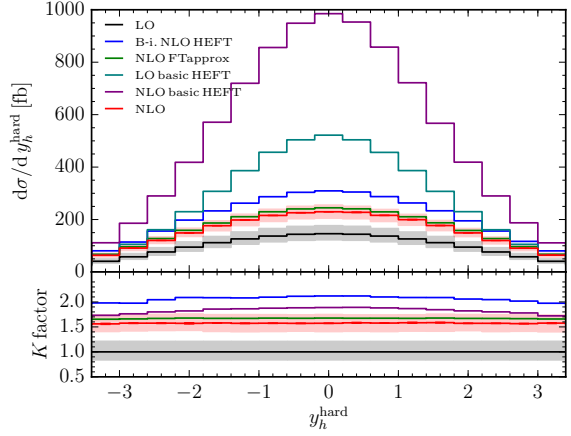
(a) 14 TeV, rapidity of the pair



(b) 14 TeV, rapidity of the leading- $p_T$  Higgs



(c) 100 TeV, rapidity of the pair



(d) 100 TeV, rapidity of the leading- $p_T$  Higgs

**Figure 8:** Rapidity distribution of the Higgs boson pair and the leading- $p_T$  Higgs boson at  $\sqrt{s} = 14$  TeV and  $\sqrt{s} = 100$  TeV.

As a first attempt to achieve this, we take the NNLO to NLO ratio from Ref. [61] and calculate

$$d\sigma^{\text{NLO-i. NNLO HEFT}} = d\sigma^{\text{NLO}} \frac{d\sigma^{\text{NNLO basic HEFT}}}{d\sigma^{\text{NLO basic HEFT}}} \quad (3.1)$$

bin by bin, where “NLO-i. NNLO HEFT” stands for NLO-improved NNLO HEFT. Results for various distributions are shown in Fig. 11. The error band is the NLO-rescaled scale uncertainty of the NNLO basic HEFT distributions, and the error on the central value is due to the error on the full NLO result. Applying the same naive rescaling on the total cross section, one obtains  $\sigma^{\text{NLO-i. NNLO HEFT}} = 38.67^{+5.2\%}_{-7.6\%}$  for 14

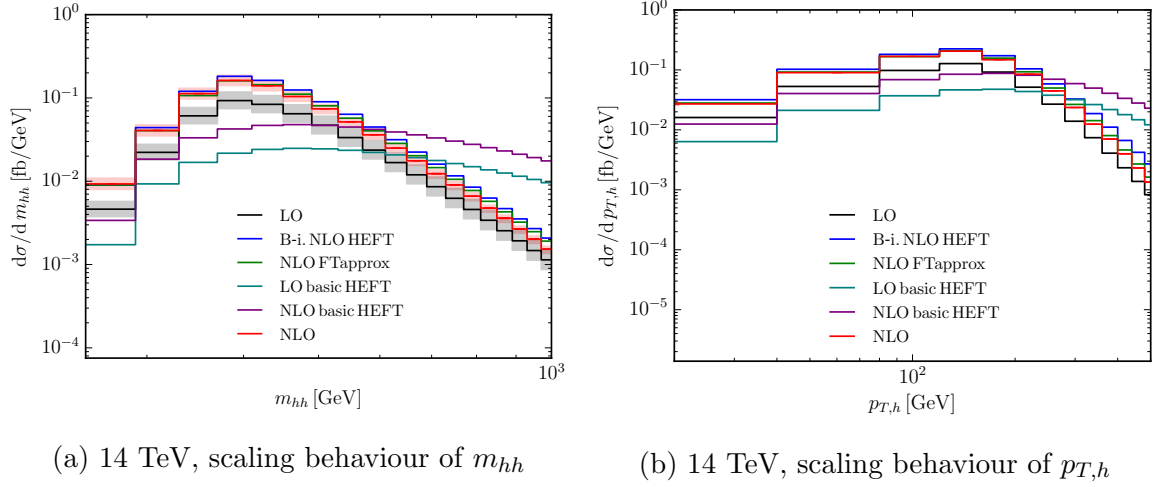


**Figure 9:** Higgs boson pair invariant mass distribution (a) and transverse momentum distribution (b) at  $\sqrt{s} = 14\text{ TeV}$  on a logarithmic scale. The different high-energy scaling behaviour of the amplitude in the full and the basic HEFT calculation can be clearly seen in the tails of the distributions.

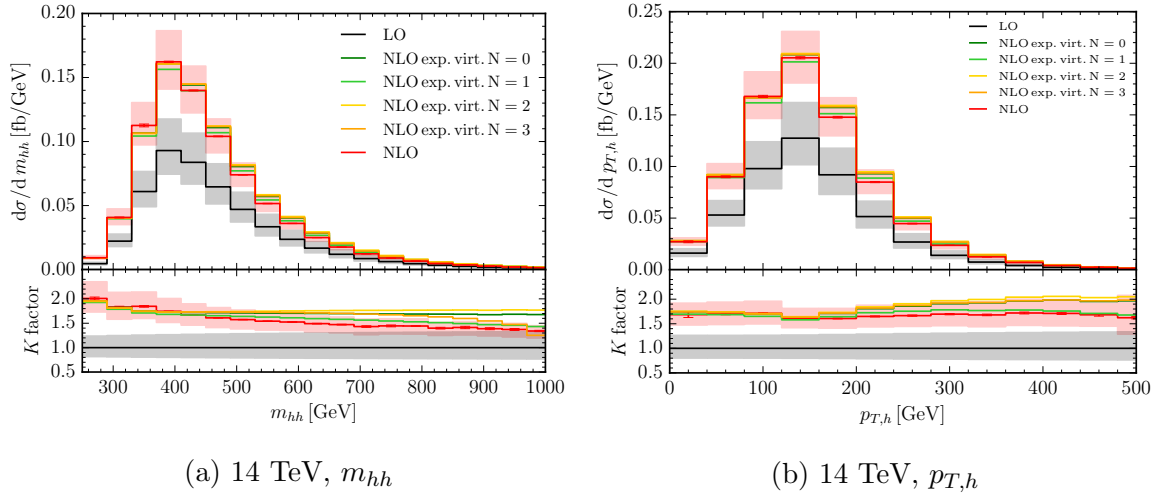


**Figure 10:** Invariant mass distribution of the Higgs boson pair (a) and  $p_T$  distribution of any Higgs (b) at  $\sqrt{s} = 14\text{ TeV}$  combining the full real emission with the virtual contribution expanded in  $1/m_t^2$  up to order  $N$ . Note that  $N = 0$  corresponds to  $\text{FT}_{\text{approx}}$ .

TeV, where we have neglected the numerical errors and simply quote the relative scale uncertainty given in Ref. [61] for the NNLO basic HEFT result.

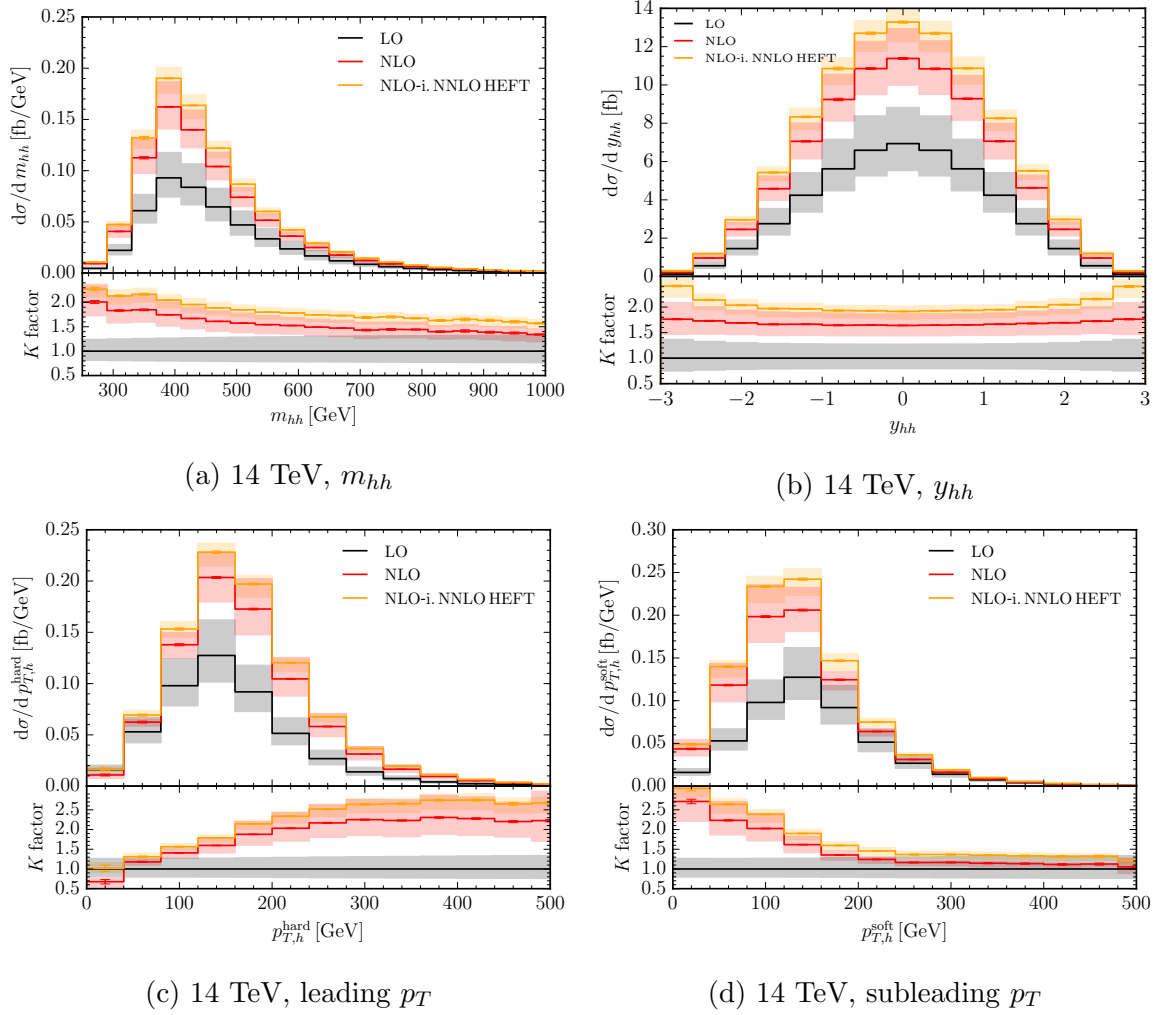


**Figure 11:** Invariant mass (a) and rapidity distribution (b) of the Higgs boson pair and transverse momentum distribution of the leading- $p_T$  (c) and the subleading- $p_T$  Higgs boson (d) at  $\sqrt{s} = 14$  TeV including the combination with the NNLO HEFT results from Ref. [61] described in the main text.

### 3.3 Sensitivity to the triple Higgs coupling

As already mentioned in Section 2.1, the Higgs boson self-coupling in the Standard Model is quite special. Not only that it is completely determined in terms of the Higgs boson mass and VEV, but it also leads to the fact that at the double Higgs production threshold  $\sqrt{\hat{s}} = 2m_h^2$ , the LO cross section is almost vanishing, due to destructive interference between box and triangle contributions. Therefore a measurement of the Higgs boson self-coupling is a very sensitive probe of New Physics effects.

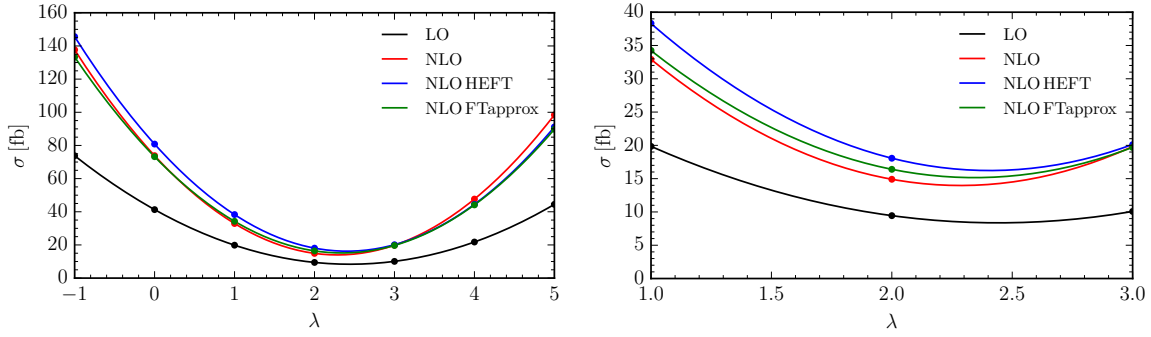


**Figure 12:** Total cross sections for various values of the triple Higgs coupling. Panel (b) zooms into the region around the minimum. The curves are the result of an interpolation of integer values for  $\lambda \in \{-1, \dots, 5\}$ .

A more complete analysis of such effects would require an approach where further operators are taken into account, for example operators which mediate direct  $t\bar{t}HH$  couplings (and Higgs-gluon couplings which can differ from the SM HEFT ones), see e.g. [37–39]. However, the conclusions drawn from the calculation of NLO corrections in the  $m_t \rightarrow \infty$  limit to the extended set of EFT Wilson coefficients have to be taken with a grain of salt, as the full top quark mass dependence may affect them considerably.

In this section we would like to focus on just a single line in the parameter space of possible non-SM Higgs couplings and investigate the behaviour of the  $m_{hh}$  distribution under variations of  $\lambda$ , where we have defined  $\lambda_{hhh} = 3m_h^2\lambda$ , see Eq. (2.7).

In Fig. 12 we show the total cross section as a function of  $\lambda$ . As already observed for the LO cross section [22], it has a minimum around  $\lambda = 2$ . Negative  $\lambda$  values, which are not excluded neither theoretically nor experimentally (within certain broad limits given e.g. by vacuum stability), do not lead to destructive interference and therefore result in a much larger cross section. For large positive values,  $\lambda \sim 5$ , the total cross section is of comparable size to the one for  $\lambda \simeq 0$ , but the shape of the  $m_{hh}$  distribution is completely different. This can be seen in Fig. 13, where we show the Higgs boson pair invariant mass distribution for various values of the Higgs boson self-coupling, at  $\sqrt{s} = 14$  TeV and  $\sqrt{s} = 100$  TeV. For  $\lambda = 5$ , the differential cross section is mainly dominated by contributions containing the Higgs boson self coupling and peaks at low  $m_{hh}$  values. In contrast, the  $\lambda = 0$  case, which does not contain any triple Higgs coupling contribution, peaks shortly beyond the  $2m_t$  threshold at  $m_{hh} \sim 400$  GeV, as does the case  $\lambda = -1$ . In the latter case, however, the total cross section is much larger. The case  $\lambda = 2$  shows a dip at  $m_{hh} \sim 300$  GeV, which is due to destructive interference effects as mentioned above. At 100 TeV, the shape of the distributions is very similar.

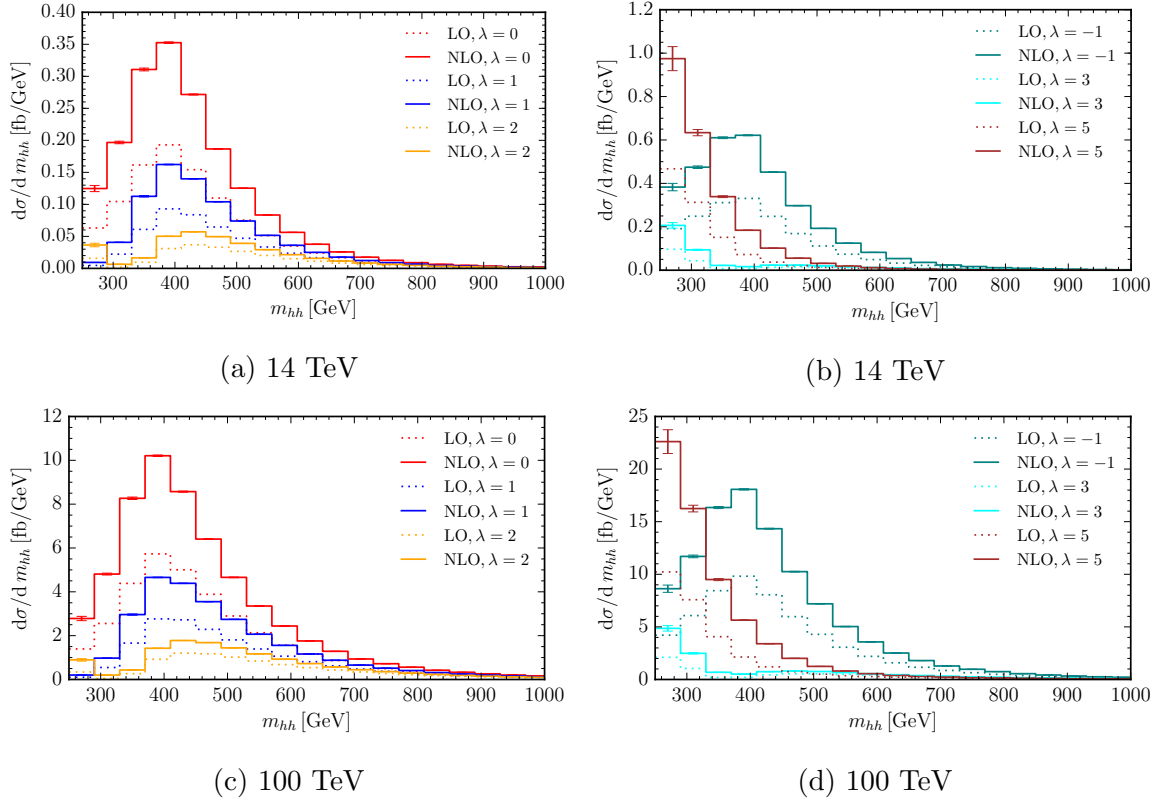
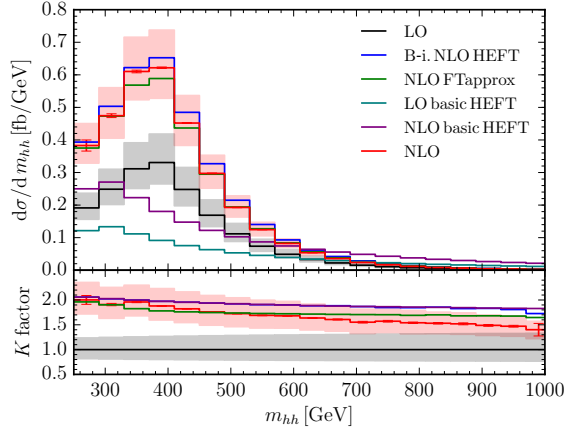


**Figure 13:** NLO and LO results with full top quark mass dependence for the  $m_{hh}$  distribution at 14 TeV and 100 TeV, for various values of the triple Higgs coupling, where  $\lambda = 1$  corresponds to the Standard Model value.

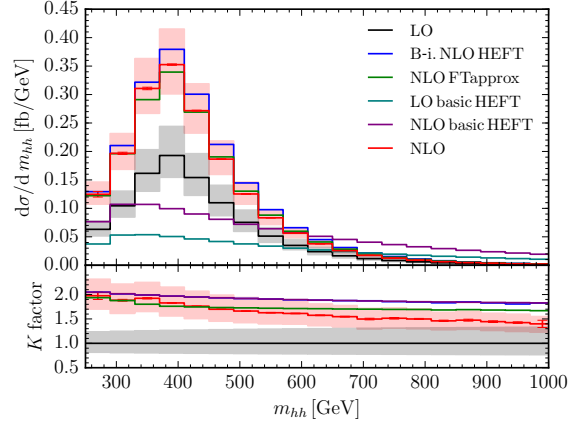
However, the fact that the cross sections are much larger can be exploited to place cuts which enlarge the sensitivity to the Higgs boson self coupling. For example, one can try to enhance the self-coupling contribution by cuts favouring highly boosted virtual Higgs bosons, decaying into a Higgs boson pair which could be detected in the  $b\bar{b}b\bar{b}$  channel. A highly boosted virtual Higgs boson must recoil against a high- $p_T$  jet. Therefore, an enhancement of the boosted component could be achieved by imposing a  $p_{T,jet}^{min}$  cut on the recoiling jet in Higgs boson pair plus jet production [110, 111]. An additional advantage of boosted Higgs bosons is the fact that they lend themselves to the use of the  $b\bar{b}b\bar{b}$  rather than the  $b\bar{b}\gamma\gamma$  decay channel, as the decay channel into  $b$ -quarks is accessible through boosted techniques. This leads to a gain in the rate which easily makes up for the loss in statistics due to a high  $p_{T,jet}^{min}$  cut.

Fig. 14 shows a comparison to the different approximations for various values of  $\lambda$ , as well as the K-factors. For all values of  $\lambda$ , the K-factors are far from being uniform,

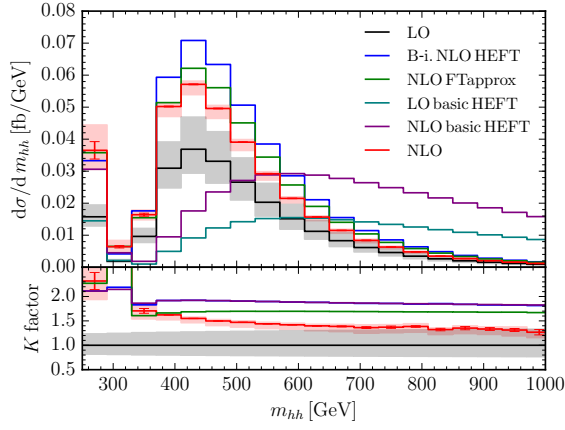
while the HEFT approximation suggests almost uniform K-factors for  $\lambda \leq 1$ . For  $\lambda = 2$ , we see a pronounced “interference dip” at  $m_{hh} \sim 330$  GeV, which is present at LO already. We can get an idea about the destructive interference effect by observing the following: In the basic HEFT approximation, the squared Born amplitude is given by Eq. (2.14). This expression has a double zero at  $\hat{s} = m_h^2(1 + 3\lambda)$ . Therefore, the re-weighting factor  $B_{FT}/B_{HEFT}$  can get large when  $B_{HEFT}$  approaches zero, i.e. at  $\sqrt{s} \simeq 330.72$  GeV for  $\lambda = 2$ ,  $\sqrt{s} \simeq 395.29$  GeV for  $\lambda = 3$ ,  $\sqrt{s} \simeq 450.7$  GeV for  $\lambda = 4$  and 500 GeV for  $\lambda = 5$ . In the full theory, the amplitude does not vanish completely at these points, but nonetheless also gets small, which should be the reason for the dips in the  $m_{hh}$  distributions for  $\lambda = 2$  and 3.



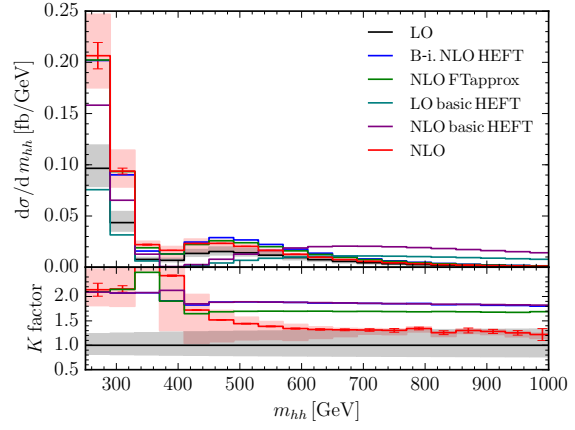
(a) 14 TeV,  $\lambda = -1$



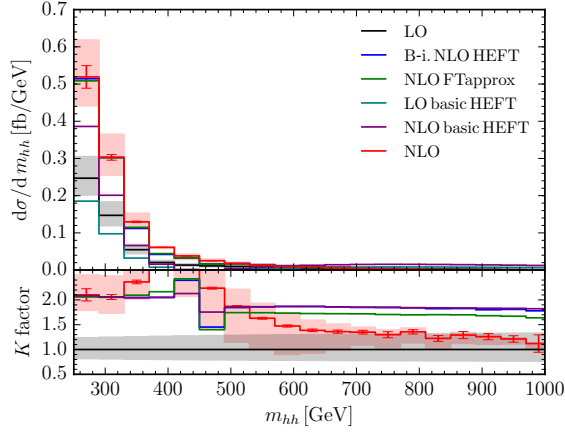
(b) 14 TeV,  $\lambda = 0$



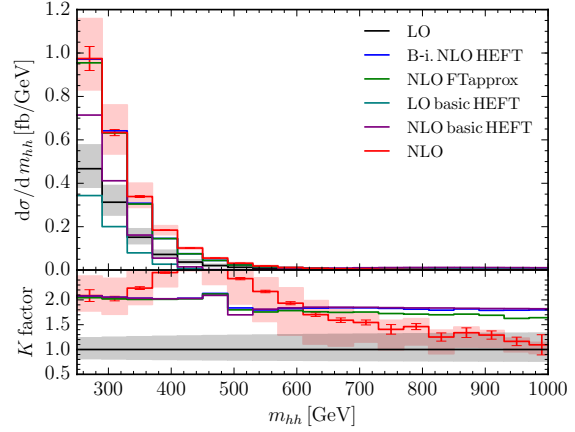
(c) 14 TeV,  $\lambda = 2$



(d) 14 TeV,  $\lambda = 3$



(e) 14 TeV,  $\lambda = 4$



(f) 14 TeV,  $\lambda = 5$

**Figure 14:** Higgs boson pair invariant mass distribution  $m_{hh}$  at  $\sqrt{s} = 14$  TeV for non-standard values of the triple Higgs coupling.



## 4 Conclusions

We have presented results of a fully differential calculation of Higgs boson pair production in gluon fusion at NLO retaining the exact top quark mass dependence. For the total cross section at  $\sqrt{s} = 14$  TeV, we found a reduction of 14% compared to the Born improved HEFT, and a 24% reduction at  $\sqrt{s} = 100$  TeV. For differential distributions, the mass effects can be even larger. In the tails of the Higgs boson transverse momentum distributions, the differences to the Born improved NLO HEFT approximation amount to more than 50%, while the  $\text{FT}_{\text{approx}}$  result, where the full top mass dependence is included only in the real radiation part, stays within 20% of the full result. The basic NLO HEFT approximation, where no reweighting by the Born result in the full theory is performed, fails to properly describe the shape of the  $m_{hh}$  and  $p_{Th}$  distributions, in particular in the tails of the distributions, where we performed an analysis of the high-energy scaling behaviour.

We also studied the influence of non-standard values for the Higgs boson self-coupling on the total cross sections and  $m_{hh}$  distributions. As is known from leading order, there is destructive interference between various contributions to the cross section, and this feature persists at NLO. Varying  $\lambda_{hhh}/\lambda_{SM}$  leads to a minimum in the value for the total cross section around  $\lambda_{hhh}/\lambda_{SM} \sim 2.3$ . The shape of the  $m_{hh}$  distribution is rather sensitive to variations of  $\lambda_{hhh}$ , which alter the interference pattern. For example, at  $\lambda_{hhh} = 0$ , the total cross section is almost as large as for  $\lambda_{hhh}/\lambda_{SM} = 5$ , but the shape of the distributions is very different.

Further, we made a first attempt to combine the full NLO results with the NNLO results calculated in the basic HEFT approximation [61] at differential distribution level, which should lead to a “NLO-improved NNLO HEFT” result, which may still be improved in the near future in various directions, for example towards Higgs boson decays.

## Acknowledgements

We are grateful to Andreas von Manteuffel for his support with the use of Reduze and to Jens Hoff for providing us results to compare to the  $1/m_t$  expansion. We also would like to thank Thomas Hahn, Stephan Jahn, Gionata Luisoni, Fabio Maltoni, Michelangelo Mangano and Magdalena Slawinska for useful discussions. This research was supported in part by the Research Executive Agency (REA) of the European Union under the Grant Agreement PITN-GA2012316704 (HiggsTools). S. Borowka gratefully acknowledges financial support by the ERC Advanced Grant MC@NNLO (340983). NG was supported by the Swiss National Science Foundation under contract

PZ00P2\_154829. GH would like to acknowledge the Kavli Institute for Theoretical Physics (KITP) for their hospitality. We gratefully acknowledge support and resources provided by the Max Planck Computing and Data Facility (MPCDF).

## References

- [1] **ATLAS** Collaboration, G. Aad et al., *Observation of a new particle in the search for the Standard Model Higgs boson with the ATLAS detector at the LHC*, *Phys. Lett. B* **716** (2012) 1–29, [[arXiv:1207.7214](#)].
- [2] **CMS** Collaboration, S. Chatrchyan et al., *Observation of a new boson at a mass of 125 GeV with the CMS experiment at the LHC*, *Phys. Lett. B* **716** (2012) 30–61, [[arXiv:1207.7235](#)].
- [3] **ATLAS, CMS** Collaboration, G. Aad et al., *Combined Measurement of the Higgs Boson Mass in  $pp$  Collisions at  $\sqrt{s} = 7$  and 8 TeV with the ATLAS and CMS Experiments*, *Phys. Rev. Lett.* **114** (2015) 191803, [[arXiv:1503.07589](#)].
- [4] **ATLAS** Collaboration, *Higgs Pair Production in the  $H(\rightarrow \tau\tau)H(\rightarrow b\bar{b})$  channel at the High-Luminosity LHC*, ATL-PHYS-PUB-2015-046, Geneva, 2015.
- [5] **ATLAS** Collaboration, *Prospects for measuring Higgs pair production in the channel  $H(\rightarrow \gamma\gamma)H(\rightarrow b\bar{b})$  using the ATLAS detector at the HL-LHC*, ATL-PHYS-PUB-2014-019, Oct, 2014.
- [6] D. Contardo, M. Klute, J. Mans, L. Silvestris, and J. Butler, *Technical Proposal for the Phase-II Upgrade of the CMS Detector*, CERN-LHCC-2015-010. LHCC-P-008. CMS-TDR-15-02, Geneva, Jun, 2015.
- [7] **ATLAS** Collaboration, *Search for Higgs boson pair production in the  $b\bar{b}\gamma\gamma$  final state using  $pp$  collision data at  $\sqrt{s} = 13$  TeV with the ATLAS detector*, ATLAS-CONF-2016-004, CERN, Geneva, Mar, 2016.
- [8] **CMS** Collaboration, V. Khachatryan et al., *Search for two Higgs bosons in final states containing two photons and two bottom quarks*, [arXiv:1603.06896](#).
- [9] **ATLAS** Collaboration, G. Aad et al., *Searches for Higgs boson pair production in the  $hh \rightarrow b\bar{b}\tau\tau, \gamma\gamma WW^*, \gamma\gamma b\bar{b}, b\bar{b}b\bar{b}$  channels with the ATLAS detector*, *Phys. Rev. D* **92** (2015) 092004, [[arXiv:1509.04670](#)].
- [10] **ATLAS** Collaboration, G. Aad et al., *Search For Higgs Boson Pair Production in the  $\gamma\gamma b\bar{b}$  Final State using  $pp$  Collision Data at  $\sqrt{s} = 8$  TeV from the ATLAS Detector*, *Phys. Rev. Lett.* **114** (2015), no. 8 081802, [[arXiv:1406.5053](#)].
- [11] **ATLAS** Collaboration, M. Aaboud et al., *Search for pair production of Higgs bosons in the  $b\bar{b}b\bar{b}$  final state using proton–proton collisions at  $\sqrt{s} = 13$  TeV with the ATLAS detector*, [arXiv:1606.04782](#).

- [12] **CMS** Collaboration, *Search for resonant pair production of Higgs bosons decaying to two bottom quark-antiquark pairs in proton-proton collisions at 13 TeV*, CMS-PAS-HIG-16-002, 2016.
- [13] **CMS** Collaboration, V. Khachatryan et al., *Search for resonant pair production of Higgs bosons decaying to two bottom quark antiquark pairs in protonproton collisions at 8 TeV*, *Phys. Lett.* **B749** (2015) 560–582, [[arXiv:1503.04114](#)].
- [14] **ATLAS** Collaboration, G. Aad et al., *Search for Higgs boson pair production in the  $b\bar{b}b\bar{b}$  final state from pp collisions at  $\sqrt{s} = 8$  TeV with the ATLAS detector*, *Eur. Phys. J.* **C75** (2015), no. 9 412, [[arXiv:1506.00285](#)].
- [15] **ATLAS** Collaboration, *Search for Higgs boson pair production in the final state of  $\gamma\gamma WW^*(\rightarrow l\nu jj)$  using  $13.3\text{ fb}^{-1}$  of pp collision data recorded at  $\sqrt{s} = 13$  TeV with the ATLAS detector*, ATLAS-CONF-2016-071, 2016.
- [16] **CMS** Collaboration, *Search for Higgs boson pair production in the  $b\bar{b}l\nu l\nu$  final state at  $\sqrt{s} = 13$  TeV*, CMS-PAS-HIG-16-024, 2016.
- [17] **CMS** Collaboration, *Search for non-resonant Higgs boson pair production in the  $b\bar{b}t\tau$  final state using 2016 data*, CMS-PAS-HIG-16-028, 2016.
- [18] **CMS** Collaboration, *Search for resonant Higgs boson pair production in the  $b\bar{b}l\nu l\nu$  final state at  $\sqrt{s} = 13$  TeV*, CMS-PAS-HIG-16-011, 2016.
- [19] **CMS** Collaboration, *Search for resonant Higgs boson pair production in the  $b\bar{b}\tau^+\tau^-$  final state*, CMS-PAS-HIG-16-013, CERN, Geneva, 2016.
- [20] **CMS** Collaboration, C. Collaboration, *Search for non-resonant Higgs boson pair production in the  $b\bar{b}\tau^+\tau^-$  final state*, CMS-PAS-HIG-16-012, 2016.
- [21] **CMS** Collaboration, *Model independent search for Higgs boson pair production in the  $b\bar{b}\tau^+\tau^-$  final state*, Tech. Rep. CMS-PAS-HIG-15-013, 2016.
- [22] J. Baglio, A. Djouadi, R. Gröber, M. M. Mühlleitner, J. Quevillon, and M. Spira, *The measurement of the Higgs self-coupling at the LHC: theoretical status*, *JHEP* **04** (2013) 151, [[arXiv:1212.5581](#)].
- [23] F. Goertz, A. Papaefstathiou, L. L. Yang, and J. Zurita, *Higgs Boson self-coupling measurements using ratios of cross sections*, *JHEP* **06** (2013) 016, [[arXiv:1301.3492](#)].
- [24] A. J. Barr, M. J. Dolan, C. Englert, and M. Spannowsky, *Di-Higgs final states augMT2ed – selecting hh events at the high luminosity LHC*, *Phys. Lett.* **B728** (2014) 308–313, [[arXiv:1309.6318](#)].
- [25] M. Gouzevitch, A. Oliveira, J. Rojo, R. Rosenfeld, G. P. Salam, and V. Sanz, *Scale-invariant resonance tagging in multijet events and new physics in Higgs pair production*, *JHEP* **07** (2013) 148, [[arXiv:1303.6636](#)].

- [26] V. Barger, L. L. Everett, C. B. Jackson, and G. Shaughnessy, *Higgs-Pair Production and Measurement of the Triscalar Coupling at LHC(8,14)*, *Phys. Lett.* **B728** (2014) 433–436, [[arXiv:1311.2931](#)].
- [27] M. J. Dolan, C. Englert, N. Greiner, and M. Spannowsky, *Further on up the road:  $hhjj$  production at the LHC*, *Phys. Rev. Lett.* **112** (2014) 101802, [[arXiv:1310.1084](#)].
- [28] P. Maierhöfer and A. Papaefstathiou, *Higgs Boson pair production merged to one jet*, *JHEP* **03** (2014) 126, [[arXiv:1401.0007](#)].
- [29] Q. Li, Q.-S. Yan, and X. Zhao, *Higgs Pair Production: Improved Description by Matrix Element Matching*, *Phys. Rev.* **D89** (2014), no. 3 033015, [[arXiv:1312.3830](#)].
- [30] M. Slawinska, W. van den Wollenberg, B. van Eijk, and S. Bentvelsen, *Phenomenology of the trilinear Higgs coupling at proton-proton colliders*, [arXiv:1408.5010](#).
- [31] D. E. Ferreira de Lima, A. Papaefstathiou, and M. Spannowsky, *Standard model Higgs boson pair production in the  $(b\bar{b})(b\bar{b})$  final state*, *JHEP* **08** (2014) 030, [[arXiv:1404.7139](#)].
- [32] R. Frederix, S. Frixione, V. Hirschi, F. Maltoni, O. Mattelaer, P. Torrielli, E. Vryonidou, and M. Zaro, *Higgs pair production at the LHC with NLO and parton-shower effects*, *Phys. Lett.* **B732** (2014) 142–149, [[arXiv:1401.7340](#)].
- [33] M. Buschmann, D. Goncalves, S. Kuttimalai, M. Schonherr, F. Krauss, and T. Plehn, *Mass Effects in the Higgs-Gluon Coupling: Boosted vs Off-Shell Production*, *JHEP* **02** (2015) 038, [[arXiv:1410.5806](#)].
- [34] M. J. Dolan, C. Englert, and M. Spannowsky, *Higgs self-coupling measurements at the LHC*, *JHEP* **10** (2012) 112, [[arXiv:1206.5001](#)].
- [35] M. J. Dolan, C. Englert, N. Greiner, K. Nordstrom, and M. Spannowsky,  *$hhjj$  production at the LHC*, *Eur. Phys. J.* **C75** (2015), no. 8 387, [[arXiv:1506.08008](#)].
- [36] M. Dall’Osso, T. Dorigo, C. A. Gottardo, A. Oliveira, M. Tosi, and F. Goertz, *Higgs Pair Production: Choosing Benchmarks With Cluster Analysis*, [arXiv:1507.02245](#).
- [37] A. Azatov, R. Contino, G. Panico, and M. Son, *Effective field theory analysis of double Higgs boson production via gluon fusion*, *Phys. Rev.* **D92** (2015), no. 3 035001, [[arXiv:1502.00539](#)].
- [38] R. Gröber, M. Mühlleitner, M. Spira, and J. Streicher, *NLO QCD Corrections to Higgs Pair Production including Dimension-6 Operators*, *JHEP* **09** (2015) 092, [[arXiv:1504.06577](#)].
- [39] M. Ghezzi, R. Gomez-Ambrosio, G. Passarino, and S. Uccirati, *NLO Higgs effective field theory and -framework*, *JHEP* **07** (2015) 175, [[arXiv:1505.03706](#)].

- [40] A. Papaefstathiou, *Discovering Higgs boson pair production through rare final states at a 100 TeV collider*, *Phys. Rev.* **D91** (2015), no. 11 113016, [[arXiv:1504.04621](#)].
- [41] D. A. Dicus, C. Kao, and W. W. Repko, *Interference effects and the use of Higgs boson pair production to study the Higgs trilinear self coupling*, [arXiv:1504.02334](#).
- [42] S. Dawson, A. Ismail, and I. Low, *What’s in the loop? The anatomy of double Higgs production*, *Phys. Rev.* **D91** (2015), no. 11 115008, [[arXiv:1504.05596](#)].
- [43] S. Dawson and I. M. Lewis, *NLO corrections to double Higgs boson production in the Higgs singlet model*, *Phys. Rev.* **D92** (2015), no. 9 094023, [[arXiv:1508.05397](#)].
- [44] J. K. Behr, D. Bortoletto, J. A. Frost, N. P. Hartland, C. Issever, and J. Rojo, *Boosting Higgs pair production in the  $b\bar{b}b\bar{b}$  final state with multivariate techniques*, *Eur. Phys. J.* **C76** (2016), no. 7 386, [[arXiv:1512.08928](#)].
- [45] G. Degrandi, P. P. Giardino, F. Maltoni, and D. Pagani, *Probing the Higgs self coupling via single Higgs production at the LHC*, [arXiv:1607.04251](#).
- [46] H. T. Li and J. Wang, *Fully Differential Higgs Pair Production in Association With a W Boson at Next-to-Next-to-Leading Order in QCD*, [arXiv:1607.06382](#).
- [47] S. Kanemura, M. Kikuchi, and K. Yagyu, *One-loop corrections to the Higgs self-couplings in the singlet extension*, [arXiv:1608.01582](#).
- [48] O. J. P. Eboli, G. C. Marques, S. F. Novaes, and A. A. Natale, *Twin Higgs Boson Production*, *Phys. Lett.* **B197** (1987) 269.
- [49] E. W. N. Glover and J. J. van der Bij, *Higgs Boson Pair Production via Gluon Fusion*, *Nucl. Phys.* **B309** (1988) 282.
- [50] T. Plehn, M. Spira, and P. M. Zerwas, *Pair production of neutral Higgs particles in gluon-gluon collisions*, *Nucl. Phys.* **B479** (1996) 46–64, [[hep-ph/9603205](#)]. [Erratum: *Nucl. Phys.* **B531**, 655(1998)].
- [51] S. Dawson, S. Dittmaier, and M. Spira, *Neutral Higgs boson pair production at hadron colliders: QCD corrections*, *Phys. Rev.* **D58** (1998) 115012, [[hep-ph/9805244](#)].
- [52] F. Maltoni, E. Vryonidou, and M. Zaro, *Top-quark mass effects in double and triple Higgs production in gluon-gluon fusion at NLO*, *JHEP* **11** (2014) 079, [[arXiv:1408.6542](#)].
- [53] J. Grigo, J. Hoff, K. Melnikov, and M. Steinhauser, *On the Higgs boson pair production at the LHC*, *Nucl. Phys.* **B875** (2013) 1–17, [[arXiv:1305.7340](#)].
- [54] J. Grigo, K. Melnikov, and M. Steinhauser, *Virtual corrections to Higgs boson pair production in the large top quark mass limit*, *Nucl. Phys.* **B888** (2014) 17–29, [[arXiv:1408.2422](#)].

- [55] J. Grigo, J. Hoff, and M. Steinhauser, *Higgs boson pair production: top quark mass effects at NLO and NNLO*, *Nucl. Phys.* **B900** (2015) 412, [[arXiv:1508.00909](#)].
- [56] G. Degrande, P. P. Giardino, and R. Grber, *On the two-loop virtual QCD corrections to Higgs boson pair production in the Standard Model*, *Eur. Phys. J.* **C76** (2016), no. 7 411, [[arXiv:1603.00385](#)].
- [57] D. de Florian and J. Mazzitelli, *Two-loop virtual corrections to Higgs pair production*, *Phys. Lett.* **B724** (2013) 306–309, [[arXiv:1305.5206](#)].
- [58] D. de Florian and J. Mazzitelli, *Higgs Boson Pair Production at Next-to-Next-to-Leading Order in QCD*, *Phys. Rev. Lett.* **111** (2013) 201801, [[arXiv:1309.6594](#)].
- [59] D. Y. Shao, C. S. Li, H. T. Li, and J. Wang, *Threshold resummation effects in Higgs boson pair production at the LHC*, *JHEP* **07** (2013) 169, [[arXiv:1301.1245](#)].
- [60] D. de Florian and J. Mazzitelli, *Higgs pair production at next-to-next-to-leading logarithmic accuracy at the LHC*, *JHEP* **09** (2015) 053, [[arXiv:1505.07122](#)].
- [61] D. de Florian, M. Grazzini, C. Hanga, S. Kallweit, J. M. Lindert, P. Maierhofer, J. Mazzitelli, and D. Rathlev, *Differential Higgs Boson Pair Production at Next-to-Next-to-Leading Order in QCD*, [arXiv:1606.09519](#).
- [62] S. Borowka, N. Greiner, G. Heinrich, S. Jones, M. Kerner, J. Schlenk, U. Schubert, and T. Zirke, *Higgs Boson Pair Production in Gluon Fusion at Next-to-Leading Order with Full Top-Quark Mass Dependence*, *Phys. Rev. Lett.* **117** (2016), no. 1 012001, erratum *ibid* 079901, [[arXiv:1604.06447](#)].
- [63] M. Jacob and G. C. Wick, *On the general theory of collisions for particles with spin*, *Annals Phys.* **7** (1959) 404–428. [*Annals Phys.*281,774(2000)].
- [64] C. Degrande, N. Greiner, W. Kilian, O. Mattelaer, H. Mebane, T. Stelzer, S. Willenbrock, and C. Zhang, *Effective Field Theory: A Modern Approach to Anomalous Couplings*, *Annals Phys.* **335** (2013) 21–32, [[arXiv:1205.4231](#)].
- [65] S. Dawson, E. Furlan, and I. Lewis, *Unravelling an extended quark sector through multiple Higgs production?*, *Phys. Rev.* **D87** (2013), no. 1 014007, [[arXiv:1210.6663](#)].
- [66] M. Spira, *Effective Multi-Higgs Couplings to Gluons*, [arXiv:1607.05548](#).
- [67] G. Cullen, N. Greiner, G. Heinrich, G. Luisoni, P. Mastrolia, et al., *Automated One-Loop Calculations with GoSam*, *Eur.Phys.J.* **C72** (2012) 1889, [[arXiv:1111.2034](#)].
- [68] G. Cullen et al., *GOSAM-2.0: a tool for automated one-loop calculations within the Standard Model and beyond*, *Eur. Phys. J.* **C74** (2014), no. 8 3001, [[arXiv:1404.7096](#)].



- [69] P. Nogueira, *Automatic Feynman graph generation*, *J.Comput.Phys.* **105** (1993) 279–289.
- [70] J. Vermaseren, *New features of FORM*, [math-ph/0010025](#).
- [71] J. Kuipers, T. Ueda, J. Vermaseren, and J. Vollinga, *FORM version 4.0*, *Comput.Phys.Commun.* **184** (2013) 1453–1467, [[arXiv:1203.6543](#)].
- [72] A. von Manteuffel and C. Studerus, *Reduze 2 - Distributed Feynman Integral Reduction*, [arXiv:1201.4330](#).
- [73] A. V. Smirnov, *FIRE5: a C++ implementation of Feynman Integral REduction*, *Comput. Phys. Commun.* **189** (2014) 182–191, [[arXiv:1408.2372](#)].
- [74] R. N. Lee, *LiteRed 1.4: a powerful tool for reduction of multiloop integrals*, *J. Phys. Conf. Ser.* **523** (2014) 012059, [[arXiv:1310.1145](#)].
- [75] M. Spira, A. Djouadi, D. Graudenz, and P. M. Zerwas, *Higgs boson production at the LHC*, *Nucl. Phys.* **B453** (1995) 17–82, [[hep-ph/9504378](#)].
- [76] R. Bonciani, P. Mastrolia, and E. Remiddi, *Vertex diagrams for the QED form-factors at the two loop level*, *Nucl. Phys.* **B661** (2003) 289–343, [[hep-ph/0301170](#)]. [Erratum: *Nucl. Phys.*B702,359(2004)].
- [77] R. Bonciani, P. Mastrolia, and E. Remiddi, *Master integrals for the two loop QCD virtual corrections to the forward backward asymmetry*, *Nucl. Phys.* **B690** (2004) 138–176, [[hep-ph/0311145](#)].
- [78] R. Harlander and P. Kant, *Higgs production and decay: Analytic results at next-to-leading order QCD*, *JHEP* **12** (2005) 015, [[hep-ph/0509189](#)].
- [79] C. Anastasiou, S. Beerli, S. Bucherer, A. Daleo, and Z. Kunszt, *Two-loop amplitudes and master integrals for the production of a Higgs boson via a massive quark and a scalar-quark loop*, *JHEP* **01** (2007) 082, [[hep-ph/0611236](#)].
- [80] T. Gehrmann, S. Guns, and D. Kara, *The rare decay  $H \rightarrow Z\gamma$  in perturbative QCD*, *JHEP* **09** (2015) 038, [[arXiv:1505.00561](#)].
- [81] R. Bonciani, V. Del Duca, H. Frellesvig, J. M. Henn, F. Moriello, and V. A. Smirnov, *Next-to-leading order QCD corrections to the decay width  $H \rightarrow Z\gamma$* , *JHEP* **08** (2015) 108, [[arXiv:1505.00567](#)].
- [82] J. Carter and G. Heinrich, *SecDec: A general program for sector decomposition*, *Comput. Phys. Commun.* **182** (2011) 1566–1581, [[arXiv:1011.5493](#)].
- [83] S. Borowka, J. Carter, and G. Heinrich, *Numerical Evaluation of Multi-Loop Integrals for Arbitrary Kinematics with SecDec 2.0*, *Comput. Phys. Commun.* **184** (2013) 396–408, [[arXiv:1204.4152](#)].

- [84] S. Borowka, G. Heinrich, S. P. Jones, M. Kerner, J. Schlenk, and T. Zirke, *SecDec-3.0: numerical evaluation of multi-scale integrals beyond one loop*, *Comput. Phys. Commun.* **196** (2015) 470–491, [[arXiv:1502.06595](#)].
- [85] A. von Manteuffel, E. Panzer, and R. M. Schabinger, *A quasi-finite basis for multi-loop Feynman integrals*, *JHEP* **02** (2015) 120, [[arXiv:1411.7392](#)].
- [86] A. von Manteuffel, E. Panzer, and R. M. Schabinger, *On the Computation of Form Factors in Massless QCD with Finite Master Integrals*, *Phys. Rev.* **D93** (2016), no. 12 125014, [[arXiv:1510.06758](#)].
- [87] S. Dittmaier, P. Uwer, and S. Weinzierl, *Hadronic top-quark pair production in association with a hard jet at next-to-leading order QCD: Phenomenological studies for the Tevatron and the LHC*, *Eur. Phys. J.* **C59** (2009) 625–646, [[arXiv:0810.0452](#)].
- [88] S. Catani and M. H. Seymour, *A General algorithm for calculating jet cross-sections in NLO QCD*, *Nucl. Phys.* **B485** (1997) 291–419, [[hep-ph/9605323](#)]. [Erratum: *Nucl. Phys.* **B510**, 503 (1998)].
- [89] D. E. Soper, *Techniques for QCD calculations by numerical integration*, *Phys. Rev.* **D62** (2000) 014009, [[hep-ph/9910292](#)].
- [90] T. Binoth, J. P. Guillet, G. Heinrich, E. Pilon, and C. Schubert, *An algebraic / numerical formalism for one-loop multi-leg amplitudes*, *JHEP* **10** (2005) 015, [[hep-ph/0504267](#)].
- [91] Z. Nagy and D. E. Soper, *Numerical integration of one-loop Feynman diagrams for N-photon amplitudes*, *Phys. Rev.* **D74** (2006) 093006, [[hep-ph/0610028](#)].
- [92] Z. Li, J. Wang, Q.-S. Yan, and X. Zhao, *Efficient Numerical Evaluation of Feynman Integral*, *Chinese Physics C* **40**, No. 3 (2016) 033103, [[arXiv:1508.02512](#)].
- [93] J. Dick, F. Y. Kuo, and I. H. Sloan, *High-dimensional integration: The quasi-monte carlo way*, *Acta Numerica* **22** (2013) 133–288.
- [94] D. Nuyens and R. Cools, *Fast algorithms for component-by-component construction of rank-1 lattice rules in shift-invariant reproducing kernel hilbert spaces*, *Mathematics of Computation* **75** (2006), no. 254 903–920.
- [95] G. P. Lepage, *VEGAS: An Adaptive Multidimensional Integration Program*, *CLNS-80/447* (1980).
- [96] S. P. Jones, *Automation of 2-loop amplitude calculations*, *PoS* **LL2016** (2016) 069, [[arXiv:1608.03846](#)].
- [97] M. Kerner, *NLO corrections to Higgs boson pair production in gluon fusion*, *PoS* **LL2016** (2016) 023, [[arXiv:1608.03851](#)].



- [98] Z. Nagy, *Next-to-leading order calculation of three jet observables in hadron hadron collision*, *Phys. Rev.* **D68** (2003) 094002, [[hep-ph/0307268](#)].
- [99] R. Harlander, T. Seidensticker, and M. Steinhauser, *Complete corrections of  $\mathcal{O}(\alpha\alpha_s)$  to the decay of the  $z$  boson into bottom quarks*, *Phys. Lett.* **B426** (1998) 125–132, [[hep-ph/9712228](#)].
- [100] T. Seidensticker, *Automatic application of successive asymptotic expansions of feynman diagrams*, [hep-ph/9905298](#).
- [101] M. Steinhauser, *MATAD: A program package for the computation of massive tadpoles*, *Comput. Phys. Commun.* **134** (2001) 335–364, [[hep-ph/0009029](#)].
- [102] R. V. Harlander, S. Liebler, and H. Mantler, *SusHi: A program for the calculation of Higgs production in gluon fusion and bottom-quark annihilation in the Standard Model and the MSSM*, *Comput. Phys. Commun.* **184** (2013) 1605–1617, [[arXiv:1212.3249](#)].
- [103] C. Anastasiou, D. de Florian, et al., *Handbook of LHC Higgs cross sections: 4. Deciphering the nature of the Higgs sector*, *Report of the LHC Higgs Cross Section Working Group* (2016).
- [104] J. Butterworth et al., *PDF4LHC recommendations for LHC Run II*, [arXiv:1510.03865](#).
- [105] S. Dulat, T.-J. Hou, J. Gao, M. Guzzi, J. Huston, P. Nadolsky, J. Pumplin, C. Schmidt, D. Stump, and C. P. Yuan, *New parton distribution functions from a global analysis of quantum chromodynamics*, *Phys. Rev.* **D93** (2016), no. 3 033006, [[arXiv:1506.07443](#)].
- [106] L. A. Harland-Lang, A. D. Martin, P. Motylinski, and R. S. Thorne, *Parton distributions in the LHC era: MMHT 2014 PDFs*, *Eur. Phys. J.* **C75** (2015), no. 5 204, [[arXiv:1412.3989](#)].
- [107] NNPDF Collaboration, R. D. Ball et al., *Parton distributions for the LHC Run II*, *JHEP* **04** (2015) 040, [[arXiv:1410.8849](#)].
- [108] F. Caola, S. Forte, S. Marzani, C. Muselli, and G. Vita, *The Higgs transverse momentum spectrum with finite quark masses beyond leading order*, [arXiv:1606.04100](#).
- [109] N. Greiner, S. Hoeche, G. Luisoni, M. Schonherr, and J.-C. Winter, *Full mass dependence in Higgs boson production in association with jets at the LHC and FCC*, [arXiv:1608.01195](#).
- [110] *We thank Michelangelo Mangano for pointing this out.*
- [111] M. L. Mangano et al., *Physics at a 100 TeV pp collider: Standard Model processes*, [arXiv:1607.01831](#).